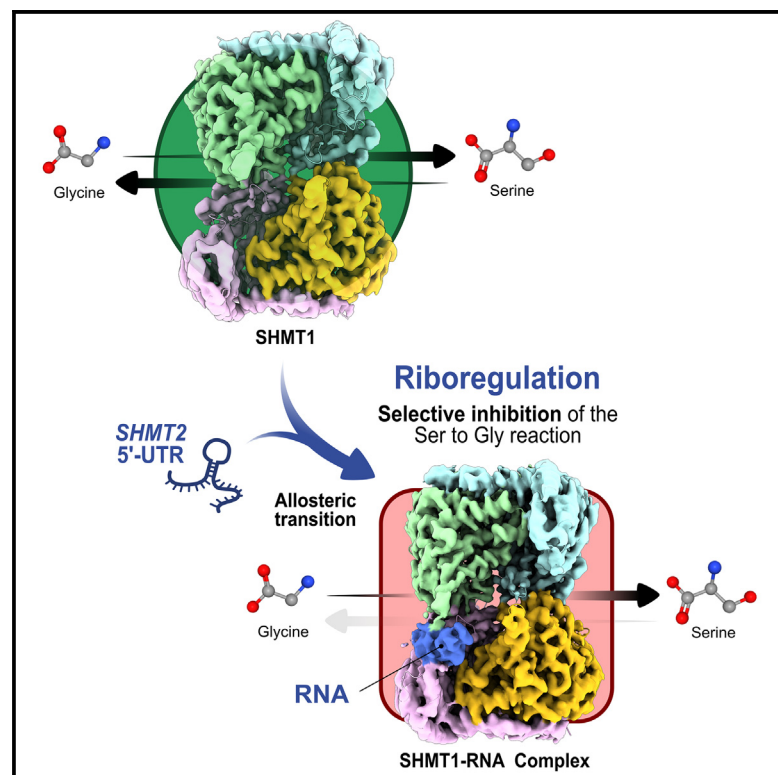# Structure-based mechanism of riboregulation of the metabolic enzyme SHMT1

## Graphical abstract



## Authors

Sharon Spizzichino, Federica Di Fonzo, Chiara Marabelli, ..., Martino Bolognesi, Giorgio Giardina, Francesca Cutruzzolà

## Correspondence

giorgio.giardina@uniroma1.it (G.G.), francesca.cutruzzola@uniroma1.it (F.C.)

## In brief

Using cryo-EM, Spizzichino et al. have solved the structure of the metabolic enzyme SHMT1 in the unbound form and in complex with RNA. Functional results showed that RNA riboregulates SHMT1 activity by acting as an allosteric switch, paving the way for the design of innovative RNA-based inhibitors.

## Highlights

- Cryo-EM structure of human SHMT1 at 3.29 Å reveals different active site conformations

- Cryo-EM structure of the SHMT1:RNA complex at 3.52 Å reveals a 4:1 binding stoichiometry

- The tetrameric assembly and a flap structural motif are necessary for RNA binding

- RNA riboregulates SHMT1 by competing with folate and acting as an allosteric switch

CellPress

**Article**

# Structure-based mechanism of riboregulation of the metabolic enzyme SHMT1

Sharon Spizzichino,[1,14] Federica Di Fonzo,[1,14] Chiara Marabelli,[2,14] Angela Tramonti,[3] Antonio Chaves-Sanjuan,[4,5] Alessia Parroni,[3] Giovanna Boumis,[1] Francesca Romana Liberati,[1,15] Alessio Paone,[1,6] Linda Celeste Montemiglio,[3] Matteo Ardini,[7] Arjen J. Jakobi,[8] Alok Bharadwaj,[8] Paolo Swuec,[9] Gian Gaetano Tartaglia,[10,11] Alessandro Paiardini,[1] Roberto Contestabile,[1] Antonello Mai,[12] Dante Rotili,[12] Francesco Fiorentino,[12] Alberto Macone,[1] Alessandra Giorgi,[1] Giancarlo Tria,[13] Serena Rinaldo,[1] Martino Bolognesi,[4,5] Giorgio Giardina,[1,*] and Francesca Cutruzzolà[1,6,16,*]

[1]Department of Biochemical Sciences, Sapienza University of Rome, P. le Aldo Moro 5, 00185 Rome, Italy
[2]Department of Molecular Medicine, University of Pavia, Via Forlanini 3, 27100 Pavia, Italy
[3]Institute of Molecular Biology and Pathology, National Research Council, P.le A. Moro 5, 00185 Rome, Italy
[4]Department of Biosciences, University of Milan, Via Celoria 26, 20133 Milano, Italy
[5]Fondazione Romeo e Enrica Invernizzi and NOLIMITS, University of Milan, Via Celoria 26, 20133 Milan, Italy
[6]Department of Biochemical Sciences, Sapienza University of Rome, Laboratory Affiliated to Istituto Pasteur Italia-Fondazione Cenci Bolognetti, P.le A. Moro 5, 00185 Rome, Italy
[7]Department of Life, Health and Environmental Sciences, University of L'Aquila, 67100 L'Aquila, Italy
[8]Department of Bionanoscience, Kavli Institute of Nanoscience Deft, Delft University of Technology, Van der Maasweg, 92629 HZ Delft, the Netherlands
[9]CryoElectron Microscopy Facility, Human Technopole, Viale Rita Levi-Montalcini 1, 20157 Milan, Italy
[10]Centre for Human Technologies (CHT), Istituto Italiano di Tecnologia (IIT), Via Enrico Melen, 83, 16152 Genova, Italy
[11]Department of Biology "Charles Darwin", Sapienza University of Rome, Piazzale Aldo Moro 5, 00185 Rome, Italy
[12]Department of Drug Chemistry and Technologies, Sapienza University of Rome, P. le Aldo Moro 5, 00185 Rome, Italy
[13]CNR Institute of Crystallography – URT Caserta c/o Dipartimento di Scienze e Tecnologie Ambientali, Biologiche e Farmaceutiche (DiSTABiF), Università degli Studi della Campania "Luigi Vanvitelli", Via Vivaldi 43, 81100 Caserta, Italy
[14]These authors contributed equally
[15]Present address: IRCCS Humanitas Research Hospital, Via Manzoni 56, 20089, Milan, Italy
[16]Lead contact
*Correspondence: giorgio.giardina@uniroma1.it (G.G.), francesca.cutruzzola@uniroma1.it (F.C.)
https://doi.org/10.1016/j.molcel.2024.06.016

## SUMMARY

RNA can directly control protein activity in a process called riboregulation; only a few mechanisms of riboregulation have been described in detail, none of which have been characterized on structural grounds. Here, we present a comprehensive structural, functional, and phylogenetic analysis of riboregulation of cytosolic serine hydroxymethyltransferase (SHMT1), the enzyme interconverting serine and glycine in one-carbon metabolism. We have determined the cryoelectron microscopy (cryo-EM) structure of human SHMT1 in its free- and RNA-bound states, and we show that the RNA modulator competes with polyglutamylated folates and acts as an allosteric switch, selectively altering the enzyme's reactivity vs. serine. In addition, we identify the tetrameric assembly and a flap structural motif as key structural elements necessary for binding of RNA to eukaryotic SHMT1. The results presented here suggest that riboregulation may have played a role in evolution of eukaryotic SHMT1 and in compartmentalization of one-carbon metabolism. Our findings provide insights for RNA-based therapeutic strategies targeting this cancer-linked metabolic pathway.

## INTRODUCTION

RNA-binding proteins (RBPs) represent a complex group of proteins, often interacting with RNA to form stable or transient ribonucleoprotein complexes through canonical RNA-binding domains (RBDs).[1–4] Over the past few years, it became clear that proteins may also bind RNA with non-canonical RBDs and that such unconventional RBPs are often involved in responding to environmental and physiological cues.[1] Intriguingly, unconventional RNA-binding

properties have been reported for enzymes involved in cellular metabolism, from glycolysis to citric acid cycle, gluconeogenesis, amino acid biosynthesis, fatty acid oxidation, lipid metabolism, and nucleotide metabolism.[5,6] The RNA:enzyme interaction is often exploited to modulate the expression of target RNAs, as in the case of aconitase/iron regulatory protein-1 (IRP1) regulating ferritin mRNA or glyceraldehyde 3-phosphate dehydrogenase (GAPDH) controlling interferon (IFN)-γ mRNA translation.[7,8] The biological significance of RNA:protein interactions lately has

been shifting from a protein-centric approach, where proteins regulate the RNA, to a more complex view, where RNA can directly affect protein structure and function, in a process called riboregulation.

Through riboregulation, RNA can control protein aggregation,[9] intracellular localization,[10] interaction with ligands, and enzymatic activity.[11] In the few mechanistic studies available on metabolic enzymes, binding of RNA and substrates were shown to be mutually exclusive events, as observed for thymidylate synthase (TYMS) and dihydrofolate reductase (DHFR), which cannot bind their cognate mRNAs in the presence of substrates.[12,13] The same concept applies to human glycolytic enzyme enolase I (ENO1), where several RNA molecules compete with the substrate molecule for binding to the enzyme active pocket.[14]

Riboregulation was shown to control the activity of human enzyme serine hydroxymethyltransferase (SHMT), a pyridoxal 5′-phosphate (PLP)-dependent enzyme involved in the folate-dependent serine/glycine interconversion in one-carbon (1-C) metabolism, a key network responsible of nucleobases biosynthesis and redox balance (Figures 1A and 1B).[15] The two major human SHMT isoforms, encoded by the serine hydroxymethyltransferase 1 (SHMT1) and SHMT2 genes, localize in the cytosol and mitochondria, respectively.[16] SHMT1 is an unconventional RBP able to bind to and control the translation of its own transcript.[17] We have shown that interaction of SHMT1 with the 5′ untranslated region (UTR) of the SHMT2 mRNA transcript lowers the expression of mitochondrial SHMT2 (Figure 1B).[15,18,19] Remarkably, the UTR2:SHMT1 interaction also riboregulates the enzymatic function in a selective manner by inhibiting the serine to glycine cleavage reaction, but not the reverse one, i.e., serine synthesis (Figure 1B).[15] Therefore, not only is the expression of SHMT2 mRNA regulated by SHMT1, but SHMT1 enzymatic activity is also selectively riboregulated by the UTR2 RNA:SHMT1 interaction. By forming the UTR2 RNA:SHMT1 complex and exploiting these two biological effects, cells can finely tune the serine-glycine metabolism across cellular compartments (cytosol and mitochondria).[20]

Understanding how the UTR2 RNA binds and controls the enzymatic activity of SHMT1 is crucial to cross-relate cytosolic and mitochondrial SHMT expression/activity. We have determined the cryoelectron microscopy (cryo-EM) structure of human SHMT1 in its free- and RNA-bound states. The structural data are complemented by *in vitro* and inhibition studies and evolutionary analyses and cellular studies. Our structure-based mechanistic study allowed us to map the RNA-binding site on SHMT1 and to highlight a conformational transition in two distinct subunits of the tetrameric enzyme, suggesting that riboregulation occurs through selective allosteric inhibition of the serine-to-glycine reaction. Moreover, we also demonstrate that to control the expression of SHMT2 mRNA in the cell, direct binding of SHMT1 to UTR2 RNA is required.

SHMTs are often highly expressed in cancer cells and their expression correlates with poor prognosis.[23–27] Despite their clinical relevance, effective small-molecule inhibitors of SHMT, able to interfere with cancer cell proliferation and metastasis formation *in vivo*, are still missing.[19,28] The results obtained in this work also provide the starting point to design effective RNA-based inhibitors of SHMT function.

## RESULTS

### Cryo-EM structure of SHMT1: The active sites of SHMT1 can assume, in the absence of substrates, both a closed and an open conformation

SHMT catalyzes the reversible conversion of serine to glycine, through a coupled reaction transforming tetrahydrofolate (THF) into N5, N10-methylene-THF (CH2-THF) (Figure 1A).

The catalytically active unit of SHMT is a dimer, containing two active sites located at the dimer interface, each site containing one PLP molecule (Figure 1C).[29–31] Eukaryotic SHMTs assemble into a tetramer (dimer of dimers) where each subunit is in equilibrium between an open and a closed state.[16,32–34] The open conformation has a more flexible and solvent-exposed active site, which becomes more rigid and buried in the closed state. The open/closed equilibrium was proposed to be differently affected by the binding of serine or glycine substrates.[32] Remarkably, the only crystal structure available of human SHMT1 shows a perfectly symmetric tetramer, each subunit being in the closed conformation (PDB: 1BJ4[22]).

The structure of the unliganded SHMT1 was determined here by single-particle cryo-EM at 3.3 Å resolution (Figure 2, Table 1, and supplemental information). No symmetry was imposed during the data processing. The four subunits are indicated as A, B, C, and D (chain ID of the PBD: 8R7H coordinates), with the A-B subunits forming one dimer and the C-D subunits forming the other (arranged in the tetramer as A-B|C-D). Surprisingly, in the SHMT1 tetrameric structure here reported, only chains A and D nicely match the closed conformation of the previously published crystal structure and display a clear density for the bound PLP and for the residues interacting with the co-factor (all the Cα of chain A and D of the cryo-EM structure superpose with the crystal structure (PDB: 1BJ4), with a root-mean-square deviation (RMSD) value for chain A (calculated on 463 over 465 of Cα atoms) of 0.91 Å and for chain D (on 456 over 465 Cα atoms) of 0.84 Å.

On the contrary, chains B and C lack density within the co-factor binding region, and their C-terminal domains are shifted to a maximum distance of 4.1 Å (RMSD values calculated on 365 Cα atoms for chain B and 344 Cα atoms for chain C, over a total length of 465 Cα atoms, are 1.13 and 1.16 Å, respectively[22]) (Figure 2). Both observations suggest that the active sites in B and C subunits are in the open conformation. We will refer to these subunits in the open state as B* and C* (Figure 2). The active site open conformation was never clearly observed within the crystallographic structures[22,29,30] possibly due to lattice restraints or to conformational selection during crystal growth. The cryo-EM results show that the active sites of SHMT1 can assume, in the absence of substrates, both the closed and open conformations, the latter previously inferred only from solution studies.[32,33,38] Given the lack of density in the subunits displaying an open conformation, PLP co-factor and its surrounding SHMT1 residues were not modeled. However, native mass spectrometry (native MS) confirmed that there are four PLP molecules per tetramer (Figure S2A), suggesting that the observed lack of density in the cryo-EM data is mainly due to the dynamics of the active site and not to dissociation of the co-factor. The SHMT1 tetrameric assembly, showing the location of the open and closed subunits (A-B*|C*-D state), as observed by cryo-EM, is shown in Figure 2.
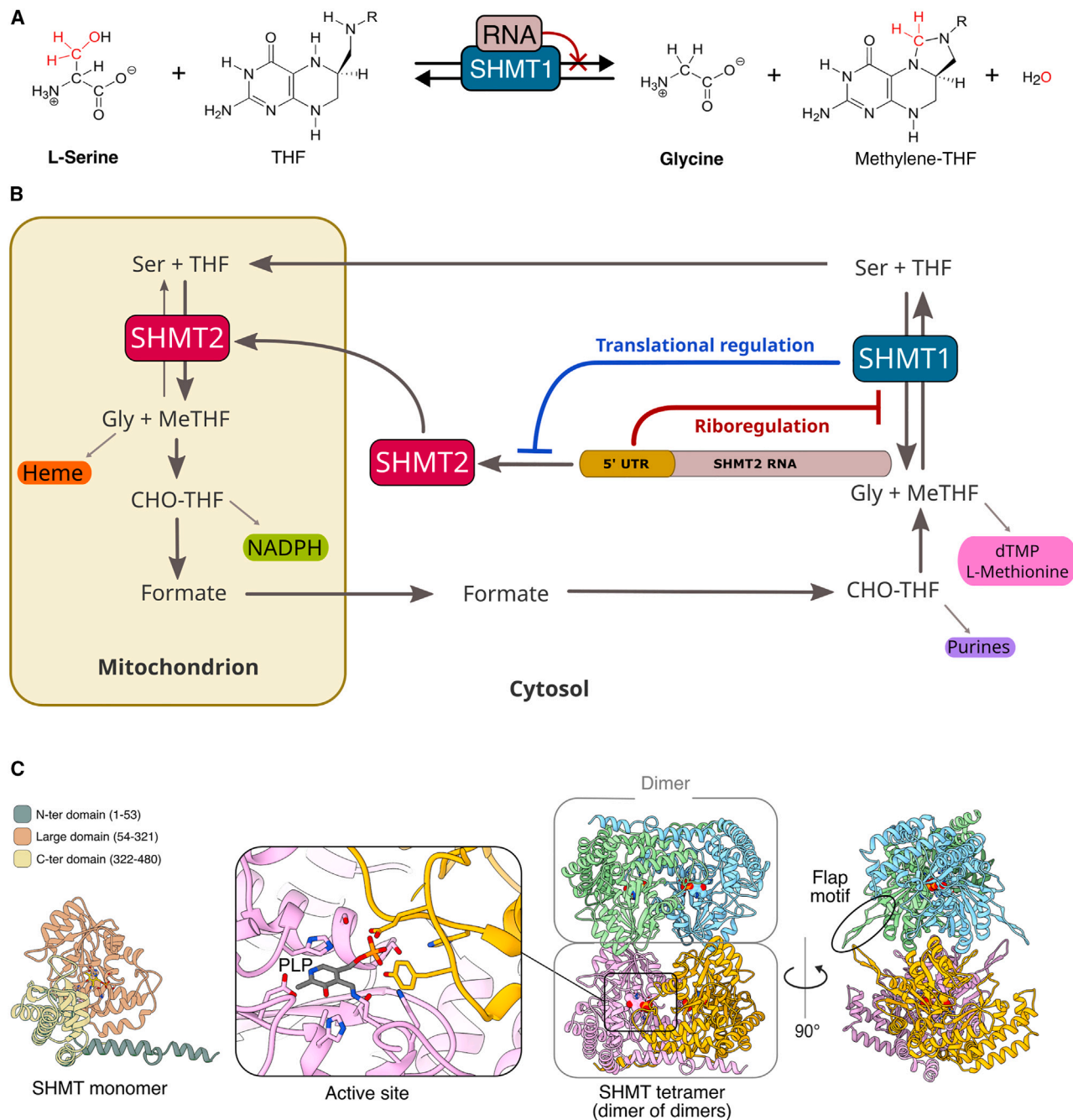
**Figure 1. Structure, catalytic activity, and RNA-dependent regulation of SHMT**

(A) Scheme of the reversible reaction catalyzed by SHMT1. RNA-binding riboregulates SHMT1 by selectively inhibiting only the serine to glycine conversion.

(B) The scheme shows the reactions catalyzed by SHMT1 and SHMT2 in the context of the folate cycle taking place between the cytosol and mitochondria.[21] The 5′ UTR of SHMT2 mRNA riboregulates SHMT1 enzymatic activity (red line); in turn, SHMT1 controls the translation of SHMT2 mRNA (blue line).[15]

(C) Quaternary structure and domain organization of human SHMT1. The enzyme is shown with each monomer differently colored (left) (crystallographic structure, PDB: 1BJ4 [22]). The PLP coenzyme (shown in gray) is located at the dimeric interface, and therefore the dimer is the minimal catalytic unit. Only one active site (out of the four ones) is highlighted in the figure. The position of the flap motif is highlighted in black.

## RNA binding induces a reorganization in the conformation of SHMT1 subunits

Our aim was to determine the structure of the SHMT1:UTR2 RNA complex, previously shown to affect serine metabolism in cells.[15,20]

In this work, considering the intrinsic flexibility of RNA molecules, we employed a 50-nt fragment (UTR2$_{1-50}$) located at 5′ end of the UTR2[15] (see STAR Methods), which efficiently binds SHMT1 and inhibits the serine to glycine reaction (Figures 3A and 3B).
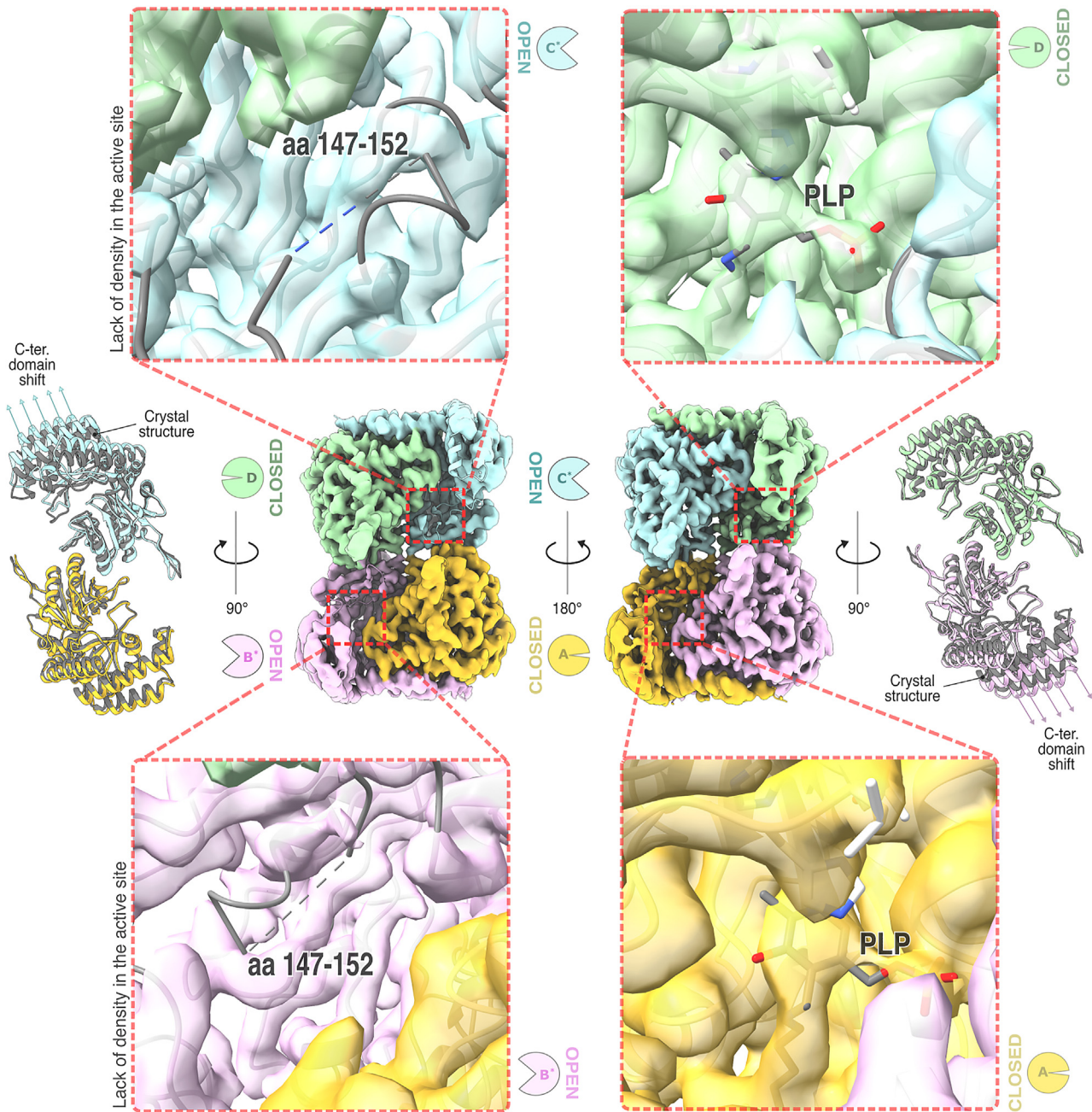
**Figure 2. Cryo-EM structure of unbound SHMT1**

Sharpened electron density map of the unbound SHMT1 (PDB: 8R7H). Chains B and C have active sites in an open conformation, whereas chains A and D have these in a closed conformation. Upper and lower: focus on the active site of each subunit. The subunits with an open conformation (on the left) show a lack of electron density in the active site region; therefore, PLP and the loop from aa 147 to aa 152 were removed from the model. Far left and right: structural superposition of each subunit of the unbound SHMT1 (different colors) with the individual subunits seen in the crystal structure (in gray: PDB: 1BJ4 [22]). Only the residues belonging to the large domain were used in the alignment to highlight the shift of the C-terminal domain of the subunits in the open conformation. For all chains, the C-terminal domains and the flap are the most dynamic regions, as observed in other PLP-dependent enzymes.[35–37]

The SHMT1:UTR2$_{1-50}$ complex was determined by cryo-EM at 3.5 Å resolution (PDB: 8A11). No symmetry was applied during the data processing. The structure of the complex displays one RNA molecule bound to the SHMT1 tetramer (Figure 3C and Table 1). This binding stoichiometry of one RNA molecule per SHMT1 tetramer was confirmed by native MS (Table S2).

The RNA molecule lies in front of one active site (subunit B), contacting the C-terminal domain of subunit B and one flap motif
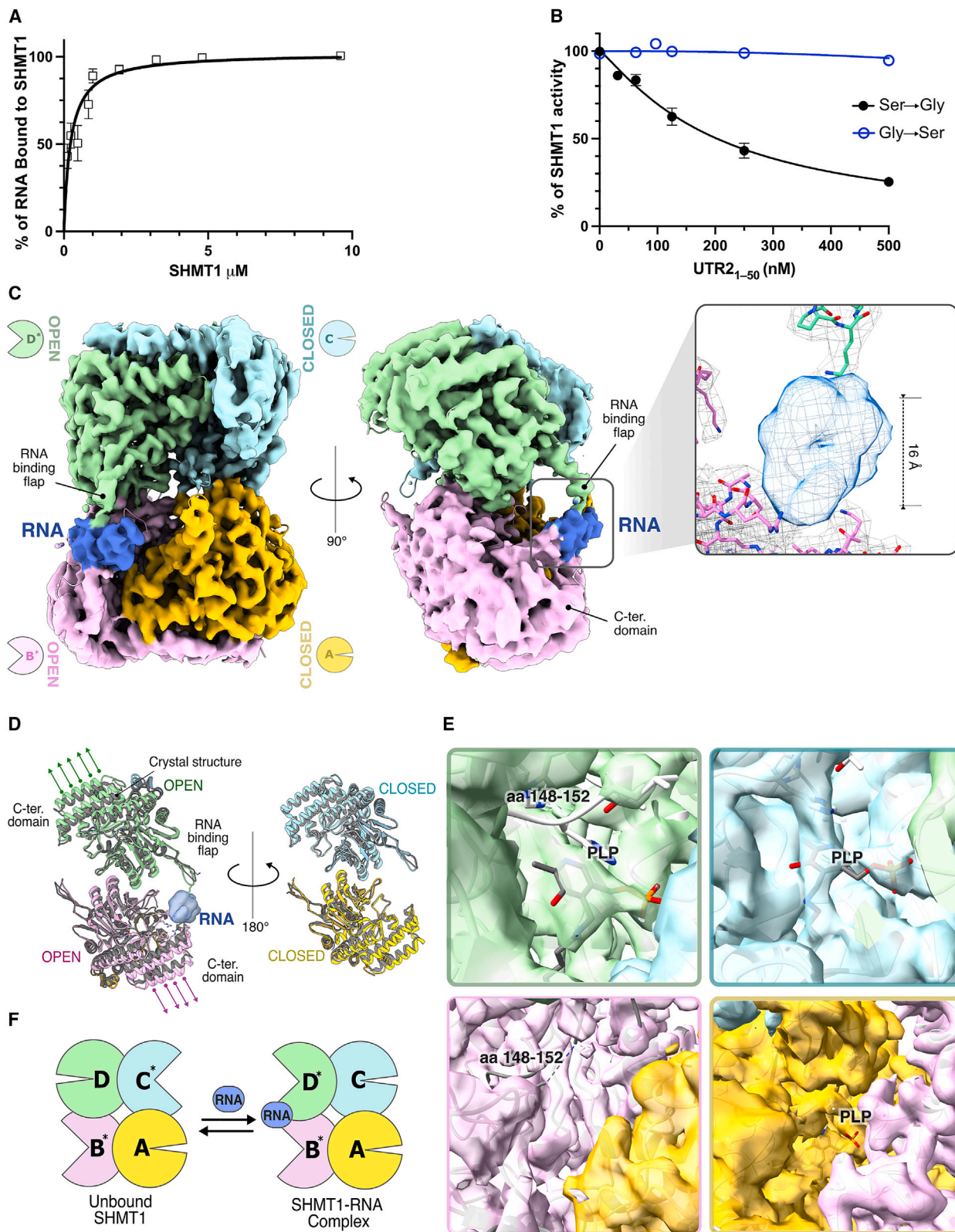
*(legend on next page)*

of the adjacent subunit D belonging to the opposite dimer (Figure 3C; Video S1). RNA binding thus requires the SHMT1 tetrameric assembly and the presence of the flap motif, a β hairpin structure composed of 13 amino acids (273-VKSVDPKTGKEIL-285), present in eukaryotic SHMT and whose function has never been fully clarified, although a recent study tried to define its role.[39] The SHMT1:RNA cryo-EM structure finally assigns a clear purpose to this motif, which will be referred to as the "RNA-binding flap."

With respect to the crystallographic structure, the two SHMT1 subunits (B and D) contacting the RNA display the following: (1) a shift of their C-terminal domains (RMSD values calculated superimposing the cryo-EM SHMT1:RNA structure and the crystal structure [PDB: 1BJ4] of ligand-free SHMT1 on 442/465 [chain A], 356/465 [chain B], 439/465 [chain C], and 377/465 [chain D] Cα atoms are 1.11, 1.24, 1.05, and 1.14 Å, respectively) (Figure 3D) and (2) a lack of density in their active site clefts (Figure 3E). The subunits can thus assume both the open and closed conformations within the SHMT1:RNA complex (Figures 3D, 3E, and S2B). In both RNA-free and RNA-bound structures, the two open subunits belong to distinct dimers; the topology of the open and closed subunits observed in the RNA-bound tetrameric SHMT1 (A-B*|C-D*) is however different from that of the unbound form, as shown in Figure 3F. In RNA-free SHMT1, the active sites in the open conformation appear to be on average more dynamic than those in the complex, according to B-factor analysis (Figure S2C), suggesting that RNA binding may affect the overall flexibility of the protein. Interestingly, RNA binds to the protein regions that oscillate most. Normal mode analysis shows that the C-terminal and flap regions are the most mobile, as the distance of the Cα-backbone of the RNA-binding flap and the C-terminal domain constantly fluctuates between 20 and 27 Å (Figure S2D; Video S2). The cryo-EM structures of SHMT1 (unbound and RNA-bound) show that the tetrameric enzyme can populate distinct quaternary states, each showing a different combination of the open/closed conformations of its active sites (Figure 3F), suggesting an RNA-dependent allosteric control of the enzyme. Allostery was previously observed in solution and in structural studies of SHMT in the presence of substrates. In titration calorimetric studies, the ligand 5-formylTHF (an unreactive THF derivative) binds with a stoichiometry of 2/tetramer and displays negative cooperativity.[34] In addition, in the crystal structure of mouse SHMT in complex with 5-formylTHF and glycine (PDB: 1EJI[29]), the folate is not bound to all four available active

sites, suggesting that, also in this case, binding of the folate to one dimer reduces the affinity for the other dimer (negative cooperativity).[29]

Based on these observations, we hypothesized that binding of RNA may decrease the conformational mobility of SHMT1 in solution and select the quaternary state of SHMT1 tetramer (A-B*|C-D*) observed here.

The observed density of the RNA was only partially defined. Map sharpening using different local-resolution algorithms failed to improve the resolution. This is likely due to the high flexibility of the nucleic acid. The observed extra density is too small to accommodate 50 nt, indicating that RNA binds in an ensemble of conformations, and most of the RNA molecule is not visible. The RNA density accounts for a maximum of six nucleotides and is in contact with the C-terminal domain and Lys279 of the RNA-binding flap (Figure 3C). A single-stranded RNA is too small to fill the gap between the C-terminal domain and the flap ($\simeq 16$ Å), whereas a double-stranded RNA would be too large. The dimensions and shape of the extra density would suggest that the anchored RNA motif falls within the hairpin region. Since the map resolution for RNA was too low to identify a unique conformation or the nucleotide sequence of the binding region, the RNA fragment was not included in the final model. The hypothesis that a hairpin loop is involved in binding was supported by experiments in solution (Figures S3A–S3C), showing that SHMT1 binds with higher affinity to single-stranded RNAs containing a hairpin loop of 12–13 nt (UTR2$_{1-50}$ and UTR2$_{1-50}$Rv), and the affinity decreases when changing the length of the loop (Figures S3A–S3C).

## Mapping the RNA-binding site on the SHMT1 tetramer

RNA binding to SHMT1 is achieved by a combination of electrostatic interactions and spatial constraints. Four lysine and three arginine residues contact or are near to the RNA docking site (Lys157, Lys158, Lys279, Lys282, Arg393, and Arg397), suggesting that electrostatic interactions play a leading role in the formation of the RNA:protein complex (Figure 4A).

Two lysine residues (Lys279 and Lys282) are located on the RNA-binding flap, whereas the arginine residues (Arg393 and Arg397) are exposed in a positively charged cleft located on the C-terminal domain (Figure 4A). Mutation of these positively charged amino acids lowers or abolishes RNA binding (Figures 4B and 4C), as shown by electrophoretic mobility shift assays (EMSAs) and native MS experiments (Figures 4B, 4C,

**Figure 3. Cryo-EM structure and analysis of the SHMT1:RNA complex**

(A) Analysis of binding affinity of UTR2$_{1-50}$ to SHMT1. All the experiments were performed three times ($n = 3$). The source data are shown in Figure S3B (upper left). The calculated apparent dissociation constant (K$_D$app) of the SHMT1:UTR2$_{1-50}$ complex is 0.23 ± 0.02 μM.

(B) UTR2$_{1-50}$ selectively inhibits the serine cleavage rection. The IC$_{50}$ of the UTR2$_{1-50}$ RNA toward the serine to glycine reaction is 203 ± 11.3 nM, whereas the glycine to serine conversion is only slightly affected. Error bars indicate standard deviation (SD) ($n = 3$).

(C) Structural features of the SHMT1-RNA complex. Sharpened electron density map of the complex (PDB: 8A11). The four subunits and the RNA (light blue) are rendered in different colors. RNA was not included in the final model due to conformational and sequence uncertainty.

(D) Structural superposition of each subunit of the SHMT1-RNA complex (different colors) with the individual subunits seen in the crystal structure (in gray: PDB: 1BJ4 [22]).

(E) Electron density in the active site region for the four subunits. PLP is labeled. In both the subunits involved in RNA binding (B* and D*), an extended region of density centered around His-148 that makes an aromatic stacking interaction with the coenzyme is either not visible or poorly defined. Therefore, we removed PLP and the loop from aa 148 to 152 in chain B and set the occupancy of those features at 50% in chain D.

(F) Comparison of the conformational topology of the unbound SHMT1 and the RNA complex. The wide aperture represents the active site in the open conformation.
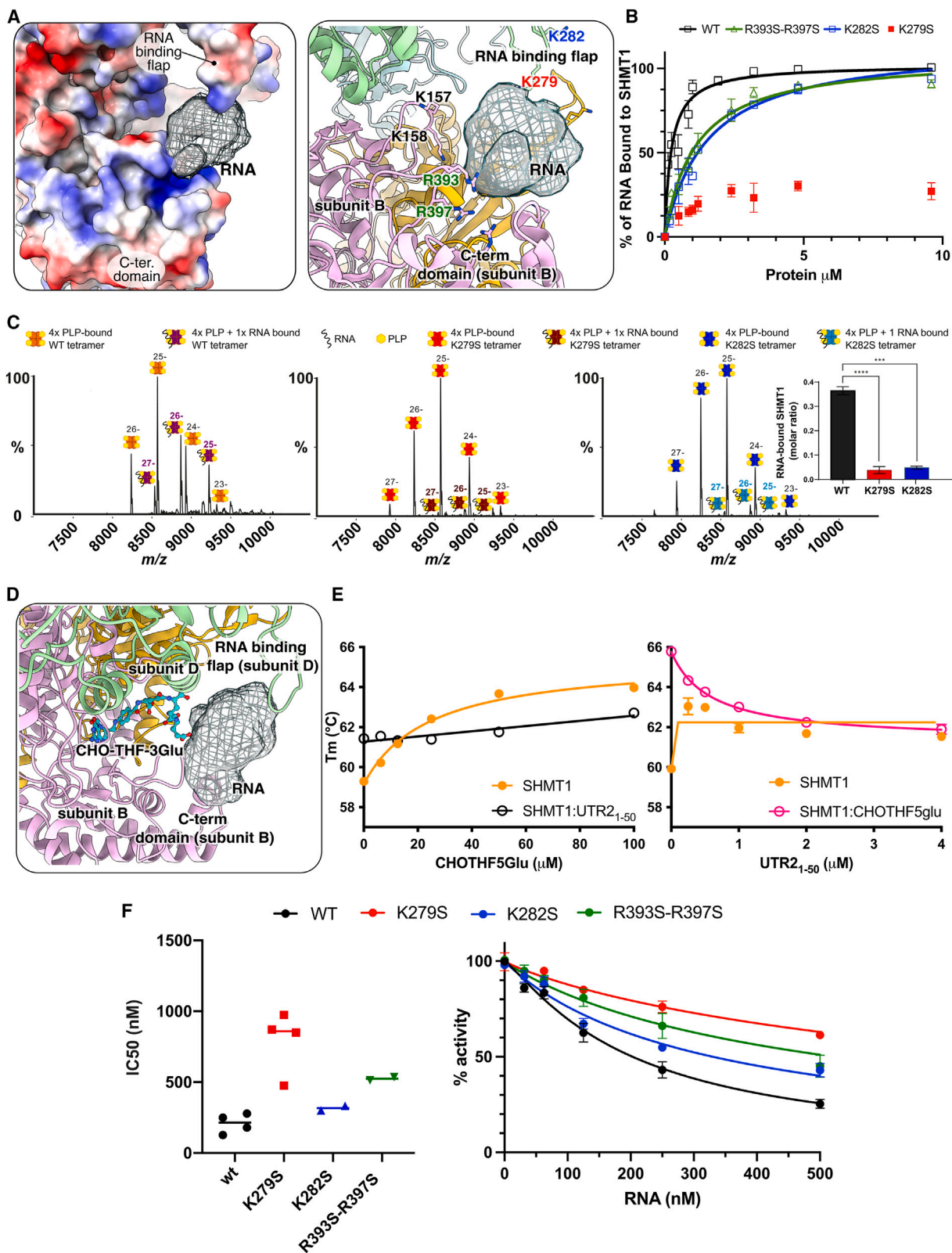
*(legend on next page)*

and S4A). These results confirm that the RNA docks between the flap and the C-terminal (Figure 4A); in agreement, limited proteolysis experiments show that UTR2$_{1-50}$ RNA protects the C-terminal domain of SHMT1 from hydrolysis (Figures S3D and S3E; Table S3).

It is interesting to note that the first run of 3D classification of the cryo-EM SHMT1:RNA particles led to the reconstruction, in addition to those classes clearly containing or not the RNA molecule, of three lower-resolution 3D classes with blurred extra densities extending from the main RNA-binding site located between the flap and the C-terminal domain (Figure S1A). However, additional refinement steps could not solve any additional extra RNA density. This suggested that the flexible RNA oligo (50 nt) can interact with the protein region surrounding the main docking site, possibly assuming multiple conformations. To confirm this hypothesis, we performed catRAPID[41] calculations of RNA-protein interaction propensity by using different stretches of the RNA 1–50 oligo and running the calculations against protein regions of 100 residues each with a 50-residue overlap. The results show a broad region of interaction centered around the SHMT1:RNA interaction site (in particular the flap), which extends in both directions at the level of the tetrameric interface (Figure S3F), in accordance with insights gained from cryo-EM processing. We thus propose that binding of RNA not only involves the primary binding site, located between the flap and the C-terminal domain, but also a network of weak interactions extending also to the adjacent potential RNA-binding site(s) on the same side of the tetramer.

### RNA competes with the binding of folate
Structural superposition of the RNA-binding site in human SHMT1 and the folate binding site from rabbit cytosolic SHMT in complex with 5-formyl-THF-3Glu (CHO-THF-3Glu)[40] shows that the RNA and folate binding sites partially overlap but do not superpose (Figure 4D). Mutation of two positively charged residues mentioned above (Lys157 and Lys158), located inside the folate binding site, was previously shown to abolish RNA binding,[15] in agreement with the structural data presented here. Binding of both RNA and folate molecules requires a tetrameric enzyme,

where two SHMT1 subunits belonging to different dimers participate in ligand recruitment (chains B and D in Figure 4D).

Interestingly, the extended binding mode of the RNA molecule to human SHMT1 proposed above resembles that observed for the polyglutamylated (polyGlu) folate substrates. These represent the physiological form of folates, with the polyGlu tail necessary to trap these metabolites within the cell[42,43] and to greatly enhance their interaction with cognate enzymes (from 5.9 μM to 20 nM).[34] In the rabbit SHMT:CHO-THF-3Glu complex, the polyGlu tail stretches out of the folate binding site and interacts with the flap residues 273–285. The folate species adopts multiple conformations in each of the two occupied binding sites, the polyGlu tail being electrostatically bound to surface cationic residues.[40]
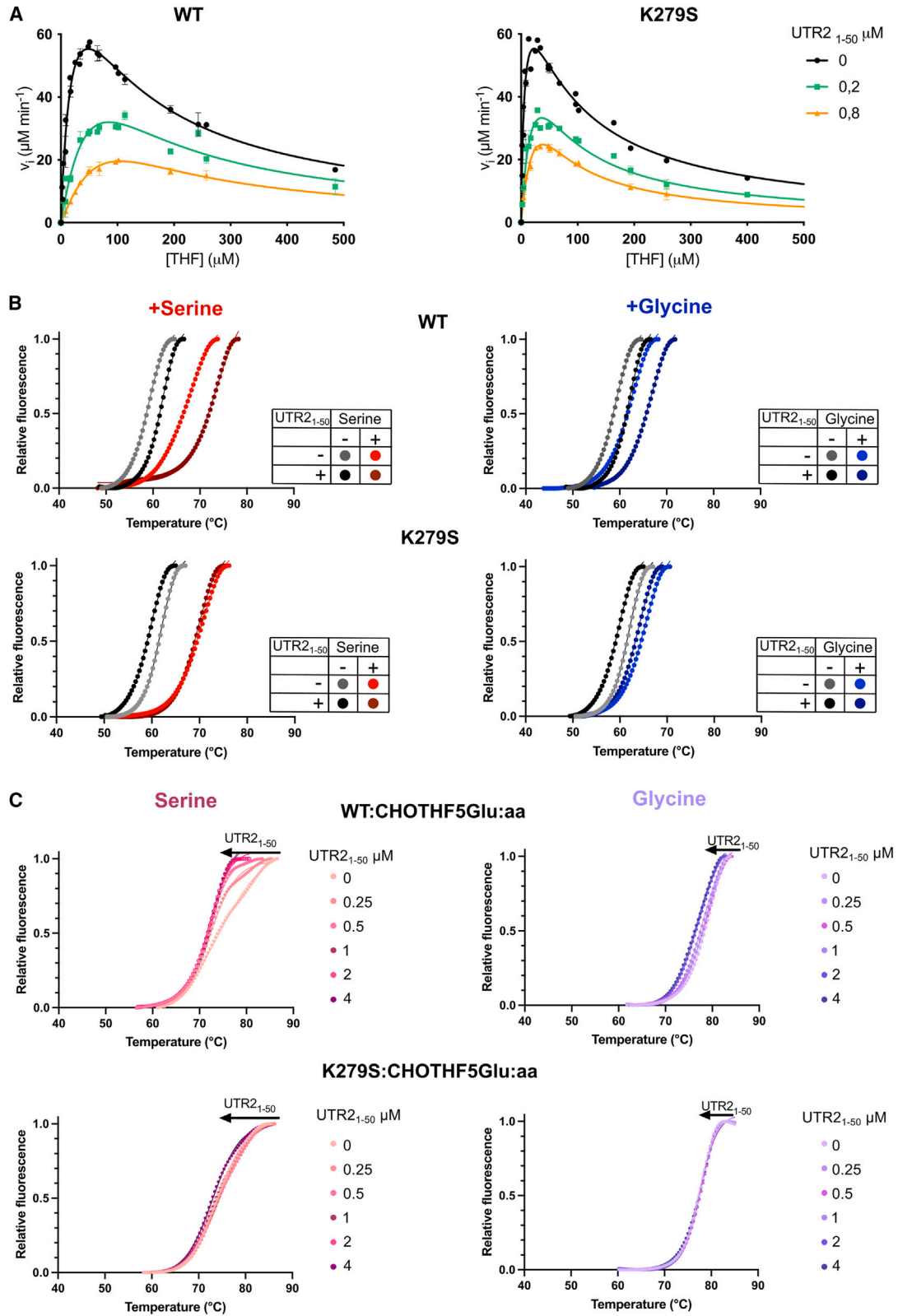
To further explore the similarities between RNA and polyGlu folates binding in solution, we analyzed the effect of RNA on the association of a pentaGlu form of folate (CHO-THF-5Glu) to SHMT1 by differential scanning fluorimetry (DSF). As shown in Figure 4E, when titrating SHMT1 with CHO-THF-5Glu, an increase in Tm is observed ($\Delta$Tm = +4.68°C ± 0.12°C, Table S4), suggesting binding of folate to the protein under these conditions. On the contrary, no significant Tm change is observed when the binding experiment is run starting from the SHMT1:RNA complex. Accordingly, addition of RNA to the SHMT1:CHO-THF-5Glu complex, leads to a decrease in Tm ($\Delta$Tm = −3.89°C ± 0.35°C, Figure 4E; Table S4), suggesting that the RNA is able to displace CHO-THF-5Glu. Mutation of selected amino acid residues, shown to affect RNA binding (Lys279, Lys282, Arg393/Arg397), results in a decreased ability of RNA to interfere with CHO-THF-5Glu binding (Figures S4C and S4D), confirming that RNA and polyGlu folate compete for the same binding site.

### Riboregulation of SHMT1: Inhibition mechanism and selectivity toward serine cleavage
Our results indicate that the SHMT1:RNA interaction requires a tetrameric assembly and the flap motif, identifying an RNA-binding site located nearby the folate binding site. To understand whether the molecular determinants of RNA binding and of riboregulation of the enzymatic activity map to the same region of the

**Figure 4. Mapping the RNA-binding region**

(A) Left: electrostatic surface potential of the RNA-binding region. RNA inserts into a positively charged cleft and is fastened against the RNA-binding flap. Right: positively charged residues in contact or in proximity to the RNA density are highlighted.

(B) Analysis of binding affinity by EMSA of the mutants of key SHMT1 residues interacting with RNA. All the experiments were performed three times ($n = 3$). The source data are shown in Figure S4A. The K$_D$app values of the protein-RNA complexes are: WT 0.23 ± 0.02 μM; K282S 1.1 ± 0.11 μM; R393S R397S 1.54 ± 0.16 μM. K$_D$app value for K279S mutant cannot be calculated given the low affinity, and only the experimental points are shown in the graph.

(C) Analysis of RNA binding to the K279S and K282S mutants by native MS. The representative mass spectra of WT (black), K279S (red), and K282S (blue) show that all proteins are in a tetrameric state with each monomer bound to one PLP molecule. The spectrum shows the binding of one RNA molecule to tetrameric WT SHMT1; binding is significantly reduced for the K279S and K282S mutants. In the experimental conditions required to perform native MS, the WT:RNA complex is less populated, as shown in Figure S2A. Both EMSA and native MS confirm a reduced RNA-binding affinity for K279S and K282S mutants with respect to WT. Values are reported in Table S2 (***$p \leq 0.001$; ****$p \leq 0.0001$).

(D) The RNA and THF binding sites on SHMT1 are in the same region. The crystal structure of rabbit SHMT1 in complex with 5-formyl-THF-3Glu (CHO-THF-3Glu) (PDB: 1LS3 [40]) was aligned with the SHMT1-RNA complex (different colors, PDB: 8A11). The RNA density is shown with gray mesh and CHO-THF-3Glu in cyan.

(E) Effect of RNA on the binding of CHO-THF-5glu probed by DSF experiments. The changes in the Tm of the protein-folate or protein-RNA complexes are plotted as a function of ligand concentration. Data were fitted with an equation describing a hyperbolic saturation behavior.

(F) The inhibitory effect of UTR2$_{1-50}$ on the mutants R279S, R282S, and the double mutant R393S-R395S. Right: inhibition curves, acquired in at least two independent experiments, were analyzed using Equation 2 to obtain the IC$_{50}$ values. Left: the plotted IC$_{50}$ values are those obtained from each individual experiment and their mean values are as follows: WT, 203 ± 11.3 nM; K279S, 903.6 ± 87.39 nM ($p \leq 0.005$); K282S, 330 ± 26 nM; R393S-R397S, 522.8 ± 75.40 nM ($p \leq 0.005$). Error bars in the figures indicate standard deviation (SD) ($n = 3$).

A

**WT**

**K279S**

UTR2 $_{1-50}$ µM
- 0
- 0,2
- 0,8

B

**+Serine**

**+Glycine**

**WT**

| UTR2$_{1-50}$ | Serine | |
|---|---|---|
| | - | + |
| - | ● | ● |
| + | ● | ● |

| UTR2$_{1-50}$ | Glycine | |
|---|---|---|
| | - | + |
| - | ● | ● |
| + | ● | ● |

**K279S**

| UTR2$_{1-50}$ | Serine | |
|---|---|---|
| | - | + |
| - | ● | ● |
| + | ● | ● |

| UTR2$_{1-50}$ | Glycine | |
|---|---|---|
| | - | + |
| - | ● | ● |
| + | ● | ● |

C

**Serine**

**WT:CHOTHF5Glu:aa**

**Glycine**

UTR2$_{1-50}$

UTR2$_{1-50}$ µM
- 0
- 0.25
- 0.5
- 1
- 2
- 4

UTR2$_{1-50}$

UTR2$_{1-50}$ µM
- 0
- 0.25
- 0.5
- 1
- 2
- 4

**K279S:CHOTHF5Glu:aa**

UTR2$_{1-50}$

UTR2$_{1-50}$ µM
- 0
- 0.25
- 0.5
- 1
- 2
- 4

UTR2$_{1-50}$

UTR2$_{1-50}$ µM
- 0
- 0.25
- 0.5
- 1
- 2
- 4

*(legend on next page)*

protein, we first established that mutation of residues Lys279, Lys282, Arg393, and Arg397 also significantly impaired the ability of RNA to inhibit SHMT1 (Figure 4F), without significantly affecting the catalytic properties (Figure S4B).

To better dissect the effect of RNA on the enzymatic activity, we confirmed that the UTR2$_{1-50}$ RNA fragment inhibits the SHMT1-catalyzed serine cleavage reaction (see Figure 1A) but has no effect on the reverse glycine-to-serine conversion (Figure 3B). By incubating the enzyme with increasing concentrations of RNA, we observed an increase in the apparent Km for THF in the serine to glycine reaction (Figure 5A left). This finding and our data presented above confirm that inhibition occurs with a partially competitive or hyperbolic mechanism, as previously suggested.[15] This type of inhibition is often characteristic of allosteric inhibitors.[44–46]

Substrate inhibition, typically observed at high THF concentration and attributed to the formation of a resting enzymatic state (the enzyme-glycine-THF dead-end complex),[47] becomes less evident after pre-incubation with RNA (Figure 5A left), suggesting again a significant influence on THF binding. On the other hand, analysis of the kinetic behavior of the K279S mutant (Figure 5A right) shows that in this mutant, the apparent Km for THF and the substrate inhibition profile are not significantly affected by RNA.

To explain the differential effect of RNA on the direct (serine to glycine) and reverse (glycine to serine) reactions catalyzed by SHMT1, we investigated the effect of RNA on the active site environment by means of ultraviolet-visible (UV-vis) spectroscopy (Figure S4E). In the first step of the reaction, the substrate amino acids react with the PLP co-factor to form spectroscopically distinct derivatives, as summarized in Figure S4F. Pre-incubation of substrate-free SHMT1 with the UTR2$_{1-50}$ RNA significantly hampered the formation of serine-bound species, being the corresponding glycine-bound adducts unaffected (Figure S4E). This indicates that serine binding, contrary to glycine, is sensitive to the conformational changes occurring upon RNA:SHMT1 complex formation. Since correct positioning of the Cβ atom of serine in the active site was previously proposed to trigger the transition from the open to the closed conformation in the enzyme subunits,[48] our results suggest that the RNA-bound enzyme is in a state that selectively interferes with productive serine binding, via Cβ atom, within the pocket.

To further compare the serine and glycine complexes of SHMT1, we analyzed the effect of the amino acids on the thermal stability of tetrameric SHMT1 through DSF and then assessed the effect of RNA. The binding of serine and glycine has a different stabilizing effect on SHMT1 (ΔTm of +7.0°C ± 0.1°C and +2.7°C ± 0.1°C, respectively, at 10 mM concentration) (Figures 5B upper and S5B left; Table S4), in agreement with literature data indicating that serine, but not glycine, triggers a conformational change when binding to the open active sites.

A different behavior between the two amino acids was also observed when they were added to the SHMT1:CHO-THF-5Glu binary complex. In the experiments with serine, an additional transition from a species with Tm = 75.7°C ± 0.2°C to a more stable one with a higher Tm (83.8°C ± 0.5°C) is observed at high serine concentration, whereas in the case of glycine an apparent two-state unfolding process is observed, regardless of glycine concentration (Tm = 78.6°C ± 0.1°C) (Figure S5C upper). In both cases, extremely stable ternary complexes (SHMT1:CHO-THF-5Glu:amino acid) are formed: the observed increase in stability is larger than the sum of the effects of individual ligands (Figure S5C; Table S4), suggesting that a change in the allosteric state of the enzyme is likely taking place when both substrates (amino acid and folate) are present. Notably, when the polyGlu tail is not associated to the folate (as for THF, CHO-THF, and lometrexol) (Figure S5D), the hyper-stabilization effect is lost for both serine and glycine, strengthening the hypothesis that this effect is linked to a change of the enzyme quaternary allosteric state requiring the extended glutamate tail to contact the flap motif.

Binding of UTR2$_{1-50}$ RNA to SHMT1 increases the Tm of about 3°C (Figure S4C upper left; Table S4), while resulting in a destabilization of the SHMT1:CHO-THF-5Glu binary complex (Figure 4E; Table S4). We then characterized the influence of RNA on the stability of the binary (SHMT1:amino acid) and ternary (SHMT1:CHO-THF-5Glu:amino acid) complexes. A differential effect of RNA is already present in the binary complexes (Figures 5B and S5A left; Table S4), but the most striking result is observed in the experiments on the ternary complexes (Figure 5C; Table S4). In the case of serine, the second transition mentioned above disappears, and the denaturation profile reverts to an apparent two-state transition; on the contrary, the denaturation profile of the ternary complex with glycine is not significantly affected. The ternary complex with glycine is

---

**Figure 5. Effect of amino acid substrates on the activity of SHMT**

(A) Inhibition of SHMT1 catalysis by RNA. Initial velocity of the WT (left) and K279S mutant (right) serine cleavage reaction was measured at different THF concentrations, in the presence of saturating L-serine (10 mM) and fixed concentrations of UTR2$_{1-50}$: 0 (black), 0.2 (green), and 0.8 (orange) μM. The continuous lines through the experimental points (average of three independent experiments) are obtained upon the least square fitting of data to Equation 3. In the presence of increasing RNA concentration, WT loses the characteristic substrate inhibition given by THF, while the kinetic profile of the K279S mutant is less affected. Error bars indicate standard deviation (SD) (*n* = 3).

(B) Binding of amino acid substrates (serine and glycine) is differentially affected by UTR2$_{1-50}$ in SHMT1 WT. DSF experiments probing the effect of serine and glycine (10 mM) on the stability of the SHMT1 and SHMT1:UTR2$_{1-50}$ complex, obtained by mixing 0.5 μM of UTR2$_{1-50}$ with 2 μM SHMT1. Binding of UTR$_{1-50}$ RNA to SHMT1 increases the Tm of about 3°C, whereas it destabilizes the K279S mutant (full titrations in Figures S5A and S5B). The K279S variant appears to be more stable in the presence of serine than the WT. Since the region containing Lys279 is positively charged, removal of one charge may render this region less dynamic, enhancing the overall stability of the mutant.

(C) Effect of increasing amounts of UTR2$_{1-50}$ (0.25–4 μM) on the stability of the ternary complex formed by mixing SHMT1 2 μM:CHO-THF-5Glu 50 μM:serine or glycine 10 mM, as measured by DSF experiments. The direction of the observed changes upon addition of RNA is indicated by an arrow. The SHMT1:CHO-THF-5glu:Ser ternary complex is destabilized upon addition of RNA; this effect is not observed for the SHMT1:CHO-THF-5glu:Gly ternary complex, nor for the K279S mutant.
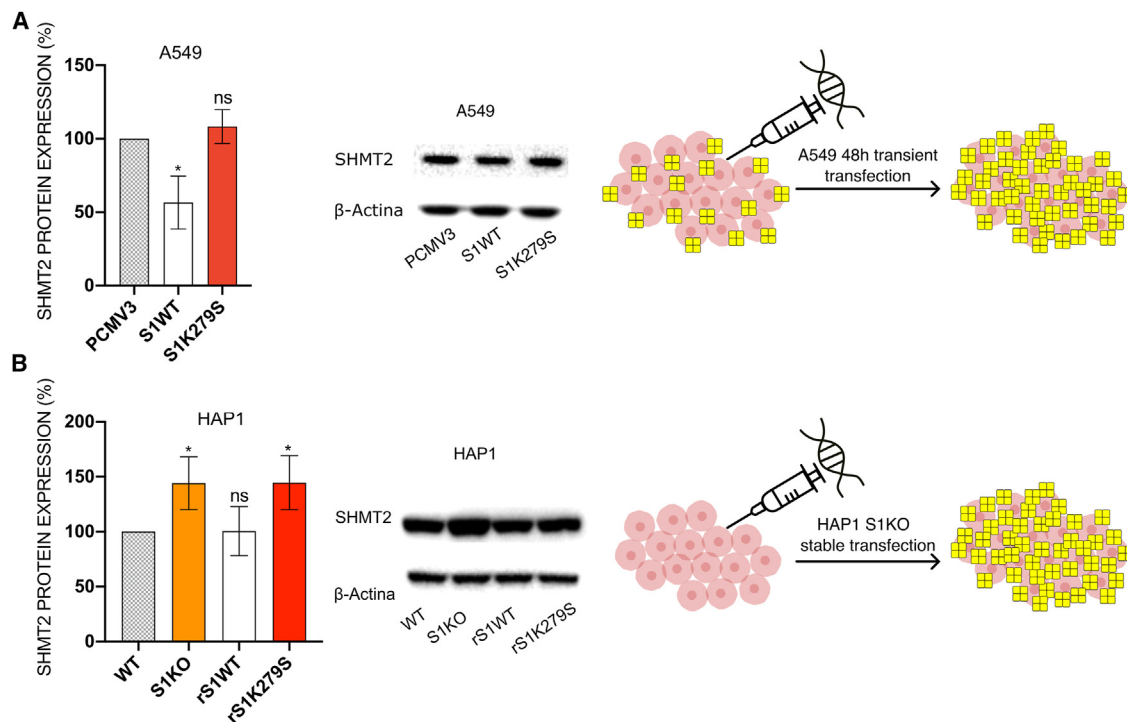
**Figure 6. Effect of SHMT1 WT and K179S mutant on the SHMT2 protein expression level**

(A) Western blot analysis of SHMT2 expression in A549 cells after 48 h transfection with the empty vector (PCMV-3, gray), SHMT1 WT (S1WT, white), and SHMT1 K279S mutant (S1K279S, red). The overexpression of SHMT1 significantly decreases the expression level of SHMT2, which is unaffected when overexpressing the K279S mutant.

(B) Western blot analysis of SHMT2 expression in HAP1 SHMT1 knockout cells (S1KO, orange) stably transfected with the plasmids mentioned above. SHMT2 levels are significantly increased with respect to HAP1 wild type (WT, gray) in S1KO. When the S1KO cells are rescued with WT protein, the SHMT2 expression level is similar to that observed for HAP1 WT, whereas when they are rescued with SHMT1 K279S, the SHMT2 protein level is significantly increased with respect to HAP1 WT and is more similar to the S1KO cells. Error bars in the figures indicate standard deviation (SD). The results were obtained by densitometric analysis of three independent biological western blot experiments ($n = 3$). In both panels, $^*p \leq 0.05$ has been considered significant, obtained by t test comparing in (A) S1WT and S1K279S to PCMV-3, and in (B) S1KO and rescued to WT. The scheme describes the experimental setup.

thus resistant to the effect of RNA. To further dissect the specific mechanism of RNA-dependent inhibition, we also characterized the K279S mutant, a SHMT1 variant which is unable to bind RNA. DSF experiments with the K279S mutant showed that the binary and ternary complexes with serine and glycine are not significantly affected by the addition of RNA (Figures 5B and 5C).

These results clearly suggest that RNA binding can modify the allosteric states populated by serine, while having a marginal effect on those populated by glycine. The RNA-dependent changes in the active site and in the allosteric state transition observed in the presence of serine, but not glycine, provide the molecular bases of the selective inhibitory effect on SHMT1 activity.

**Translational regulation of SHMT2 expression by SHMT1**

The effect of the selective riboregulation of SHMT1 activity in cells was already demonstrated in a previous publication,[20] showing that transfection of H1299 adenocarcinoma cell lines with the UTR2 fragment alone or with full-length SHMT2 mRNA leads to an increase of intracellular serine, due to the selective RNA-mediated inhibition of the cytosolic serine

to glycine reaction (Figure 1). The structural and functional data presented above provided the starting point to demonstrate that SHMT1 selectively regulates SHMT2 mRNA translation in cells. We employed two different experimental setups to determine whether the K279S mutant, unable to bind RNA, was still effective in regulating SHMT2 protein expression (Figure 6). In the first experiment, we transiently transfected A549 lung adenocarcinoma cells with constructs overexpressing either SHMT1 wild-type (WT) or the K279S mutant (Figure 6A). The results show that overexpression of WT SHMT1 downregulates SHMT2 protein levels, while overexpression of the K279S mutant does not. This evidence was also confirmed in HAP1 leukemia cells stably knocked out for SHMT1 gene (S1KO) (Figure 6B). The levels of SHMT2 protein in S1KO cells were compared with those observed in S1KO cells complemented with the cDNA of either SHMT1 WT or the K279S mutant. Only the transfection with the cDNA of SHMT1 WT, but not of SHMT1 K279S, lowered the expression of SHMT2 protein (Figure 6B). These results demonstrate that formation of the SHMT1:RNA complex is required to selectively regulate the translation of SHMT2 transcript in a cellular context.

**Table 1. Cryo-EM data collection, image processing, and model refinement statistics**

| Data collection and image processing | | |
|---|---|---|
| Structure | SHMT1 | SHMT1-RNA |
| Microscope | TALOS Arctica | |
| Voltage (kV) | 200 | |
| Camera | Falcon 3EC | |
| Magnification | ×120,000 | |
| Total electron dose (e⁻/Å²) | 40.0 | |
| Defocus range (μm) | −0.5 and −2.5 μm | |
| Pixel size (Å) | 0.889 | |
| Micrographs (no.) | 5,450 | |
| Symmetry imposed | C1 | C1 |
| Initial particle images (no.) | 4,980,852 | |
| Final particle images (no.) | 76,723 | 94,430 |
| Resolution (Å) (FSC threshold) | 3.29 (0.143) | 3.52 (0.143) |
| Sharpening B-factor (Å²) | −115.4 | −127.7 |
| EMDB code | – | 15,065 |
| Model refinement | | |
| Protein residues | 1,850 | 1,875 |
| RNA nucleotides | 0 | 0 |
| PLP molecules | 2 | 3 |
| Root-mean-square deviations (RMSDs) | | |
| Bond lengths (Å) | 0.002 | 0.002 |
| Bond angles (°) | 0.421 | 0.451 |
| Ramachandran plot | | |
| Favored (%) | 97.87 | 97.46 |
| Allowed (%) | 2.13 | 2.49 |
| Disallowed (%) | 0.00 | 0.05 |
| Validation | | |
| Molprobity score | 1.36 | 1.45 |
| Clashscore | 6.08 | 6.22 |
| CC (mask) | 0.85 | 0.75 |
| CC (box) | 0.90 | 0.87 |
| CC (peaks) | 0.90 | 0.65 |
| CC (volume) | 0.84 | 0.73 |
| PDB code | 8R7H | 8A11 |

## DISCUSSION

Metabolic reprogramming allows cells to adapt to intrinsic or extrinsic cues. This involves high flexibility in nutrient acquisition and utilization,[26,49] as well as control of the activity and expression of metabolic enzymes by allosteric effectors (metabolites or small molecules) and by upstream signaling pathways. The discovery of the RNA-binding properties of metabolic enzymes suggested that RNA can control the activity and expression of these proteins, and it thus controls metabolic changes.

Here, we elucidated the molecular bases of the RNA-based mechanism controlling the activity and expression of the meta-bolic enzymes SHMT1 and SHMT2. We provide evidence that RNA may act as a dynamic metabolic "switch" by directly affecting the activity of the metabolic enzyme(s) either by competing with substrates and/or by shifting the equilibrium of allosteric states (see scheme in Figure S7B).

The SHMT1:RNA complex is characterized by a high degree of conformational flexibility of both partners, in keeping with the concept that RNA structural dynamics plays a key role in guiding its cellular functions.[48,50] The main RNA docking site observed in the cryo-EM structure includes a flap motif and the C-terminal domain. The formation of this RNA:protein complex not only selectively controls the enzyme activity, as detailed above, but also the translation of the target RNA coding for SHMT2, as proved in a cellular context. Although the present work is focused on the effect of UTR2 RNA, further studies will be required to clarify whether SHMT1 can bind other RNA targets in the cell and what the consequences are for cell behavior.

More in general, unveiling the structural features of unconventional RNA-protein complexes is mandatory to define general rules on where and how RNA can bind and govern the enzymatic activity. It is still largely unknown how other RNA-binding metabolic enzymes (including mitochondrial SHMT) and their cognate RNA regulators interact. In addition, given that many RNA-binding metabolic enzymes do not contain canonical RNA-binding motifs, prediction of the binding regions proved to be difficult. Therefore, determination of the structure of the RNA:protein complexes is highly required to design effective RNA regulators to control RBP enzymes and metabolic reprogramming. These RNAs could be employed as drugs for therapeutic intervention in cancer and other pathological states, targeting SHMT1 and possibly other metabolic enzymes having RNA-binding properties.

In parallel, our results also contribute to clarifying a more fundamental yet equally fascinating issue, i.e., how RNA molecules had concurred in the emergence of new metabolic abilities and metabolic routes. RNA:metabolic enzyme pairs might have co-evolved to control the fate of selected metabolites and the direction of metabolic fluxes, thus suggesting a possible explanation of how the complexity of metabolism might have risen during evolution.[51–53] In lung cancer cells, the consequence of increasing the level of UTR2 RNA species that bind to SHMT1 (i.e., the SHMT2 mRNA) is the separation of glycine and serine utilization between the cytosolic and mitochondrial compartments, through the two enzyme isoforms.[20] In mitochondria, SHMT2 catalyzes the serine to glycine reaction and sustains the production of 1-C units yielding formate, which is then exported to the cytosol. Therefore, the folate mitochondrial pool should be kept high to meet the metabolic demand of THF by SHMT2. Based on the results presented here, we propose that riboregulation of SHMT1 has two parallel and physiologically relevant effects: (1) it favors the glycine to serine conversion in the cytosol to increase the serine levels available for mitochondrial 1-C metabolism; and (2) it can limit THF entrapment in the SHMT1 dead-end complex (as seen in the inhibition studies presented here), thus simultaneously increasing the THF levels available for SHMT2. To further assess the possible contribution of this RNA:protein interaction to the evolution of metabolic routes, we carried out a systematic phylogenetic analysis starting from the Archaean eon. The phylogenesis of SHMT

(Figures S6 and S7A; Table S5) suggests that the tetrameric quaternary structure and the flap motif required for the RNA:protein interaction co-evolved with the compartmentalization of 1-C metabolism between cytoplasm and mitochondria, confirming that the RNA-binding ability of metabolic enzymes might offer a sophisticated way to control metabolic routes also across compartments.

### Limitations of the study

We describe here the structural basis of the interaction and RNA-mediated control of cytosolic SHMT, which will be used as a starting point to design tailored-made RNA molecules able to control its activity. Although the overall resolution of the SHMT1:RNA complex was 3.5 Å, the resolution of the RNA density was too low to identify the nucleotide sequence of the binding region, and map sharpening using different local-resolution algorithms failed to improve the resolution. Therefore, we have decided not to include the RNA fragment in the final model. The experiments described in the paper on the features of the RNA ligand were aimed at better interpreting the density seen in the map, not at finding out the molecular determinants of specificity; the latter would have required analysis of the features of other RNA ligands able to bind and regulate SHMTs in the cells. Finally, although measuring the effect of SHMT1 mutations on relevant metabolite levels was outside the scope of the present study, additional experiments could be implemented to clarify this aspect of the metabolic response to regulatory RNAs.

### STAR★METHODS

Detailed methods are provided in the online version of this paper and include the following:

- KEY RESOURCES TABLE
- RESOURCE AVAILABILITY
  - Lead contact
  - Materials availability
  - Data and code availability
- EXPERIMENTAL MODEL AND STUDY PARTICIPANT DETAILS
  - Cell lines culture and transfection
- METHOD DETAILS
  - Protein expression and purification
  - Site directed mutagenesis
  - Cryo-EM grid preparation and data acquisition
  - Single-particle data processing
  - Local scale map sharpening
  - Model building
  - catRAPID
  - EMSA assays
  - Activity assays
  - Spectral measurements of SHMT1-amino acid complexes
  - Differential Scanning Fluorimetry (DSF)
  - Native MS analysis
  - Trypsin digestion
  - Protein extracts, SDS-PAGE and Western Blotting
  - Phylogenetic Analysis
- QUANTIFICATION AND STATISTICAL ANALYSIS

### SUPPLEMENTAL INFORMATION

Supplemental information can be found online at https://doi.org/10.1016/j.molcel.2024.06.016.

### REFERENCES

1. Hentze, M.W., Castello, A., Schwarzl, T., and Preiss, T. (2018). A brave new world of RNA-binding proteins. Nat. Rev. Mol. Cell Biol. *19*, 327–341. https://doi.org/10.1038/nrm.2017.130.

2. Li, X., Kazan, H., Lipshitz, H.D., and Morris, Q.D. (2014). Finding the target sites of RNA-binding proteins. Wiley Interdiscip. Rev. RNA *5*, 111–130. https://doi.org/10.1002/WRNA.1201.

3. Biamonti, G., and Riva, S. (1994). New insights into the auxiliary domains of eukaryotic RNA binding proteins. FEBS Lett. *340*, 1–8. https://doi.org/10.1016/0014-5793(94)80162-2.

4. Corley, M., Burns, M.C., and Yeo, G.W. (2020). How RNA binding proteins interact with RNA: molecules and mechanisms. Mol. Cell *78*, 9–29. https://doi.org/10.1016/J.MOLCEL.2020.03.011.

5. Nagy, E., and Rigby, W.F.C. (1995). Glyceraldehyde-3-phosphate dehydrogenase selectively binds AU-rich RNA in the NAD+-binding region

(Rossmann fold) (*). J. Biol. Chem. *270*, 2755–2763. https://doi.org/10.1074/JBC.270.6.2755.

6. Castello, A., Hentze, M.W., and Preiss, T. (2015). Metabolic enzymes enjoying new partnerships as RNA-binding proteins. Trends Endocrinol. Metab. *26*, 746–757. https://doi.org/10.1016/j.tem.2015.09.012.

7. Volz, K. (2008). The functional duality of iron regulatory protein 1. Curr. Opin. Struct. Biol. *18*, 106–111. https://doi.org/10.1016/J.SBI.2007.12.010.

8. Millet, P., Vachharajani, V., McPhail, L., Yoza, B., and McCall, C.E. (2016). GAPDH binding to TNF-α mRNA contributes to post-transcriptional repression in monocytes: A novel mechanism of communication between inflammation and metabolism. J. Immunol. *196*, 2541–2551. https://doi.org/10.4049/JIMMUNOL.1501345.

9. Horos, R., Büscher, M., Kleinendorst, R., Alleaume, A.M., Tarafder, A.K., Schwarzl, T., Dziuba, D., Tischer, C., Zielonka, E.M., Adak, A., et al. (2019). The small non-coding vault RNA1-1 acts as a Riboregulator of autophagy. Cell *176*, 1054–1067.e12. https://doi.org/10.1016/j.cell.2019.01.030.

10. Zhu, Y., Jin, L., Shi, R., Li, J., Wang, Y., Zhang, L., Liang, C.Z., Narayana, V.K., De Souza, D.P., Thorne, R.F., et al. (2022). The long noncoding RNA glycoLINC assembles a lower glycolytic metabolon to promote glycolysis. Mol. Cell *82*, 542–554.e6. https://doi.org/10.1016/J.MOLCEL.2021.11.017.

11. Kerr, A.G., Wang, Z., Wang, N., Kwok, K.H.M., Jalkanen, J., Ludzki, A., Lecoutre, S., Langin, D., Bergo, M.O., Dahlman, I., et al. (2022). The long noncoding RNA ADIPINT regulates human adipocyte metabolism via pyruvate carboxylase. Nat. Commun. *13*, 2958. https://doi.org/10.1038/s41467-022-30620-0.

12. Chu, E., and Allegra, C.J. (1996). The role of thymidylate synthase as an RNA binding protein. BioEssays *18*, 191–198. https://doi.org/10.1002/BIES.950180306.

13. Chu, E., Takimoto, C.H., Voeller, D., Grem, J.L., and Allegra, C.J. (1993). Specific binding of human dihydrofolate reductase protein to dihydrofolate reductase messenger RNA in vitro. Biochemistry *32*, 4756–4760. https://doi.org/10.1021/BI00069A009.

14. Huppertz, I., Perez-Perri, J.I., Mantas, P., Sekaran, T., Schwarzl, T., Russo, F., Ferring-Appel, D., Koskova, Z., Dimitrova-Paternoga, L., Kafkia, E., et al. (2022). Riboregulation of Enolase 1 activity controls glycolysis and embryonic stem cell differentiation. Mol. Cell *82*, 2666–2680.e11. https://doi.org/10.1016/J.MOLCEL.2022.05.019.

15. Guiducci, G., Paone, A., Tramonti, A., Giardina, G., Rinaldo, S., Bouzidi, A., Magnifico, M.C., Marani, M., Menendez, J.A., Fatica, A., et al. (2019). The moonlighting RNA-binding activity of cytosolic serine hydroxymethyltransferase contributes to control compartmentalization of serine metabolism. Nucleic Acids Res. *47*, 4240–4254. https://doi.org/10.1093/nar/gkz129.

16. Garrow, T.A., Brenner, A.A., Whitehead, V.M., Chen, X.N., Duncan, R.G., Korenberg, J.R., and Shane, B. (1993). Cloning of human cDNAs encoding mitochondrial and cytosolic serine hydroxymethyltransferases and chromosomal localization. J. Biol. Chem. *268*, 11910–11916. https://doi.org/10.1016/S0021-9258(19)50286-1.

17. Liu, X., Reig, B., Nasrallah, I.M., and Stover, P.J. (2000). Human cytoplasmic serine hydroxymethyltransferase is an mRNA binding protein. Biochemistry *39*, 11523–11531. https://doi.org/10.1021/BI000665D.

18. Paone, A., Marani, M., Fiascarelli, A., Rinaldo, S., Giardina, G., Contestabile, R., Paiardini, A., and Cutruzzolà, F. (2014). SHMT1 knockdown induces apoptosis in lung cancer cells by causing uracil misincorporation. Cell Death Dis. *5*, e1525. https://doi.org/10.1038/cddis.2014.482.

19. Giardina, G., Paone, A., Tramonti, A., Lucchi, R., Marani, M., Magnifico, M.C., Bouzidi, A., Pontecorvi, V., Guiducci, G., Zamparelli, C., et al. (2018). The catalytic activity of serine hydroxymethyltransferase is essential for de novo nuclear dTMP synthesis in lung cancer cells. FEBS Journal *285*, 3238–3253. https://doi.org/10.1111/febs.14610.

20. Monti, M., Guiducci, G., Paone, A., Rinaldo, S., Giardina, G., Liberati, F.R., Cutruzzolá, F., and Tartaglia, G.G. (2021). Modelling of SHMT1 riboregulation predicts dynamic changes of serine and glycine levels across cellular compartments. Comput. Struct. Biotechnol. J. *19*, 3034–3041. https://doi.org/10.1016/J.CSBJ.2021.05.019.

21. Tramonti, A., Nardella, C., di Salvo, M.L., Barile, A., Cutruzzolá, F., and Contestabile, R. (2018). Human cytosolic and mitochondrial serine hydroxymethyltransferase isoforms in comparison: full kinetic characterization and substrate inhibition properties. Biochemistry *57*, 6984–6996. https://doi.org/10.1021/ACS.BIOCHEM.8B01074.

22. Renwick, S.B., Snell, K., and Baumann, U. (1998). The crystal structure of human cytosolic serine hydroxymethyltransferase: A target for cancer chemotherapy. Structure *6*, 1105–1116. https://doi.org/10.1016/S0969-2126(98)00112-9.

23. Zhang, P., and Yang, Q. (2021). Overexpression of SHMT2 predicts a poor prognosis and promotes tumor cell growth in bladder cancer. Front. Genet. *12*, 682856. https://doi.org/10.3389/fgene.2021.682856.

24. Jain, M., Nilsson, R., Sharma, S., Madhusudhan, N., Kitami, T., Souza, A.L., Kafri, R., Kirschner, M.W., Clish, C.B., and Mootha, V.K. (2012). Metabolite profiling identifies a key role for glycine in rapid cancer cell proliferation. Science *336*, 1040–1044. https://doi.org/10.1126/SCIENCE.1218595.

25. Antonov, A., Agostini, M., Morello, M., Minieri, M., Melino, G., Amelio, I., Antonov, A., Agostini, M., Morello, M., and Minieri, M. (2014). Bioinformatics analysis of the serine and glycine pathway in cancer cells. Oncotarget *5*, 11004–11013. https://doi.org/10.18632/ONCOTARGET.2668.

26. Amelio, I., Cutruzzolá, F., Antonov, A., Agostini, M., and Melino, G. (2014). Serine and glycine metabolism in cancer. Trends Biochem. Sci. *39*, 191–198. https://doi.org/10.1016/J.TIBS.2014.02.004.

27. Gu, J., Li, X., Li, H., Jin, Z., and Jin, J. (2019). MicroRNA-198 inhibits proliferation and induces apoptosis by directly suppressing FGFR1 in gastric cancer. Biosci. Rep. *39*, BSR20181258. https://doi.org/10.1042/BSR20181258.

28. Paiardini, A., Tramonti, A., Schirch, D., Guiducci, G., di Salvo, M.L., Fiascarelli, A., Giorgi, A., Maras, B., Cutruzzolà, F., and Contestabile, R. (2016). Differential 3-bromopyruvate inhibition of cytosolic and mitochondrial human serine hydroxymethyltransferase isoforms, key enzymes in cancer metabolic reprogramming. Biochim. Biophys. Acta *1864*, 1506–1517. https://doi.org/10.1016/J.BBAPAP.2016.08.010.

29. Szebenyi, D.M.E., Liu, X., Kriksunov, I.A., Stover, P.J., and Thiel, D.J. (2000). Structure of a murine cytoplasmic serine hydroxymethyltransferase quinonoid ternary complex: evidence for asymmetric obligate dimers. Biochemistry *39*, 13313–13323. https://doi.org/10.1021/BI000635A.

30. Scarsdale, J.N., Kazanina, G., Radaev, S., Schirch, V., and Wright, H.T. (1999). Crystal structure of rabbit cytosolic serine hydroxymethyltransferase at 2.8 Å resolution: mechanistic implications. Biochemistry *38*, 8347–8358. https://doi.org/10.1021/bi9904151.

31. Zanetti, K.A., and Stover, P.J. (2003). Pyridoxal phosphate inhibits dynamic subunit interchange among serine hydroxymethyltransferase tetramers. J. Biol. Chem. *278*, 10142–10149. https://doi.org/10.1074/jbc.M211569200.

32. Stover, P., and Schirch, V. (1991). 5-formyltetrahydrofolate polyglutamates are slow tight binding inhibitors of serine hydroxymethyltransferase. J. Biol. Chem. *266*, 1543–1550. https://doi.org/10.1016/S0021-9258(18)52328-0.

33. Stover, P., and Schirch, V. (1992). Enzymatic mechanism for the hydrolysis of 5,10-Methenyltetrahydropteroylglutamate to 5-formyltetrahydropteroylglutamate by serine hydroxymethyltransferase. Biochemistry *31*, 2155–2164. https://doi.org/10.1021/bi00122a037.

34. Huang, T., Wang, C., Maras, B., Barra, D., and Schirch, V. (1998). Thermodynamic analysis of the binding of the polyglutamate chain of 5-Formyltetrahydropteroylpolyglutamates to serine hydroxymethyltransferase. Biochemistry *37*, 13536–13542. https://doi.org/10.1021/bi980827u.

35. Spizzichino, S., Pampalone, G., Dindo, M., Bruno, A., Romani, L., Cutruzzolà, F., Zelante, T., Pieroni, M., Cellini, B., and Giardina, G. (2022). Crystal structure of Aspergillus fumigatus AroH, an aromatic amino acid aminotransferase. Proteins 90, 435–442. https://doi.org/10.1002/prot.26234.

36. Giardina, G., Montioli, R., Gianni, S., Cellini, B., Paiardini, A., Voltattorni, C.B., and Cutruzzolà, F. (2011). Open conformation of human DOPA decarboxylase reveals the mechanism of PLP addition to Group II decarboxylases. Proc. Natl. Acad. Sci. USA 108, 20514–20519. https://doi.org/10.1073/pnas.1111456108.

37. Dindo, M., Pascarelli, S., Chiasserini, D., Grottelli, S., Costantini, C., Uechi, G.I., Giardina, G., Laurino, P., and Cellini, B. (2022). Structural dynamics shape the fitness window of alanine:glyoxylate aminotransferase. Protein Sci. 31, e4303. https://doi.org/10.1002/PRO.4303.

38. Schirch, V., and Szebenyi, D.M.E. (2005). Serine hydroxymethyltransferase revisited. Curr. Opin. Chem. Biol. 9, 482–487. https://doi.org/10.1016/j.cbpa.2005.08.017.

39. Ubonprasert, S., Jaroensuk, J., Pornthanakasem, W., Kamonsutthipaijit, N., Wongpituk, P., Mee-udorn, P., Rungrotmongkol, T., Ketchart, O., Chitnumsub, P., Leartsakulpanich, U., et al. (2019). A flap motif in human serine hydroxymethyltransferase is important for structural stabilization, ligand binding, and control of product release. J. Biol. Chem. 294, 10490–10502. https://doi.org/10.1074/JBC.RA119.007454.

40. Fu, T.F., Scarsdale, J.N., Kazanina, G., Schirch, V., and Wright, H.T. (2003). Location of the pteroylpolyglutamate-binding site on rabbit cytosolic serine hydroxymethyltransferase. J. Biol. Chem. 278, 2645–2653. https://doi.org/10.1074/jbc.M210649200.

41. Bellucci, M., Agostini, F., Masin, M., and Tartaglia, G.G. (2011). Predicting protein associations with long noncoding RNAs. Nat. Methods 8, 444–445. https://doi.org/10.1038/NMETH.1611.

42. Stover, P.J., and Field, M.S. (2011). Trafficking of intracellular folates. Adv. Nutr. 2, 325–331. https://doi.org/10.3945/AN.111.000596.

43. Zeng, H., Chen, Z.-S., Belinsky, M.G., Rea, P.A., and Kruh, G.D. (2001). Transport of methotrexate (MTX) and folates by multidrug resistance protein (MRP) 3 and MRP1: effect of polyglutamylation on MTX transport. Cancer Res. 61, 7225–7232.

44. Cornish-Bowden, A. (1995). Fundamentals of Enzyme Kinetics, Revised Edition (Portland Press Ltd.).

45. Monod, J., Changeux, J.P., and Jacob, F. (1963). Allosteric proteins and cellular control systems. J. Mol. Biol. 6, 306–329. https://doi.org/10.1016/S0022-2836(63)80091-1.

46. Barlow, J.N., Conrath, K., and Steyaert, J. (2009). Substrate-dependent modulation of enzyme activity by allosteric effector antibodies. Biochim. Biophys. Acta 1794, 1259–1268. https://doi.org/10.1016/J.BBAPAP.2009.03.019.

47. Amornwatcharapong, W., Maenpuen, S., Chitnumsub, P., Leartsakulpanich, U., and Chaiyen, P. (2017). Human and Plasmodium serine hydroxymethyltransferases differ in rate-limiting steps and pH-dependent substrate inhibition behavior. Arch. Biochem. Biophys. 630, 91–100. https://doi.org/10.1016/J.ABB.2017.07.017.

48. Vicens, Q., and Kieft, J.S. (2022). Thoughts on how to think (and talk) about RNA structure. Proc. Natl. Acad. Sci. USA 119, e2112677119. https://doi.org/10.1073/pnas.2112677119.

49. Hanahan, D., and Weinberg, R.A. (2011). Hallmarks of cancer: the next generation. Cell 144, 646–674. https://doi.org/10.1016/j.cell.2011.02.013.

50. Ganser, L.R., Kelly, M.L., Herschlag, D., and Al-Hashimi, H.M. (2019). The roles of structural dynamics in the cellular functions of RNAs. Nat. Rev. Mol. Cell Biol. 20, 474–489. https://doi.org/10.1038/S41580-019-0136-0.

51. Ralser, M. (2014). The RNA world and the origin of metabolic enzymes. Biochem. Soc. Trans. 42, 985–988. https://doi.org/10.1042/BST20140132.

52. Kirschning, A. (2021). Coenzymes and their role in the evolution of life. Angew. Chem. Int. Ed. Engl. 60, 6242–6269. https://doi.org/10.1002/ANIE.201914786.

53. Giacobelli, V.G., Fujishima, K., Lepšík, M., Tretyachenko, V., Kadavá, T., Makarov, M., Bednárová, L., Novák, P., and Hlouchová, K. (2022). In vitro evolution reveals noncationic protein–RNA interaction mediated by metal ions. Mol. Biol. Evol. 39, msac032. https://doi.org/10.1093/MOLBEV/MSAC032.

54. Zivanov, J., Nakane, T., Forsberg, B.O., Kimanius, D., Hagen, W.J.H., Lindahl, E., and Scheres, S.H.W. (2018). New tools for automated high-resolution cryo-EM structure determination in RELION-3. eLife 7, e42166. https://doi.org/10.7554/eLife.42166.

55. Adams, P.D., Afonine, P.V., Bunkóczi, G., Chen, V.B., Davis, I.W., Echols, N., Headd, J.J., Hung, L.-W., Kapral, G.J., Grosse-Kunstleve, R.W., et al. (2010). Phenix: a comprehensive Python-based system for macromolecular structure solution. Acta Crystallogr. D Biol. Crystallogr. 66, 213–221. https://doi.org/10.1107/S0907444909052925.

56. Emsley, P., Lohkamp, B., Scott, W.G., and Cowtan, K. (2010). Features and development of coot. Acta Crystallogr. D Biol. Crystallogr. 66, 486–501. https://doi.org/10.1107/S0907444910007493.

57. Pettersen, E.F., Goddard, T.D., Huang, C.C., Couch, G.S., Greenblatt, D.M., Meng, E.C., and Ferrin, T.E. (2004). UCSF Chimera—A visualization system for exploratory research and analysis. J. Comput. Chem. 25, 1605–1612. https://doi.org/10.1002/JCC.20084.

58. Spizzichino, S., Boi, D., Boumis, G., Lucchi, R., Liberati, F.R., Capelli, D., Montanari, R., Pochetti, G., Piacentini, R., Parisi, G., et al. (2022). Cytosolic localization and in vitro assembly of human de novo thymidylate synthesis complex. FEBS Journal 289, 1625–1649. https://doi.org/10.1111/FEBS.16248.

59. Rohou, A., and Grigorieff, N. (2015). CTFFIND4: fast and accurate defocus estimation from electron micrographs. J. Struct. Biol. 192, 216–221. https://doi.org/10.1016/J.JSB.2015.08.008.

60. Rosenthal, P.B., and Henderson, R. (2003). Optimal determination of particle orientation, absolute hand, and contrast loss in single-particle electron cryomicroscopy. J. Mol. Biol. 333, 721–745. https://doi.org/10.1016/J.JMB.2003.07.013.

61. Jakobi, A.J., and Bharadwaj, A. (2022). LocScale – reference-based local sharpening of cryo-EM maps (2.0). Zenodo. https://doi.org/10.5281/zenodo.6652013.

62. Bharadwaj, A., and Jakobi, A.J. (2022). Electron scattering properties of biological macromolecules and their use for cryo-EM map sharpening. Faraday Discuss. 240, 168–183. https://doi.org/10.1039/d2fd00078d.

63. Sato, K., Hamada, M., Asai, K., and Mituyama, T. (2009). CentroidFold: a web server for RNA secondary structure prediction. Nucleic Acids Res. 37, W277–W280. https://doi.org/10.1093/NAR/GKP367.

64. Do, C.B., Woods, D.A., and Batzoglou, S. (2006). CONTRAfold: RNA secondary structure prediction without physics-based models. Bioinformatics 22, e90–e98. https://doi.org/10.1093/BIOINFORMATICS/BTL246.

65. Sato, K., Kato, Y., Hamada, M., Akutsu, T., and Asai, K. (2011). IPknot: fast and accurate prediction of RNA secondary structures with pseudoknots using integer programming. Bioinformatics 27, i85–i93. https://doi.org/10.1093/BIOINFORMATICS/BTR215.

66. Bellaousov, S., Reuter, J.S., Seetin, M.G., and Mathews, D.H. (2013). RNAstructure: web servers for RNA secondary structure prediction and analysis. Nucleic Acids Res. 41, W471–W474. https://doi.org/10.1093/NAR/GKT290.

67. Zakov, S., Goldberg, Y., Elhadad, M., and Ziv-Ukelson, M. (2011). Rich parameterization improves RNA structure prediction. J. Comput. Biol. 18, 1525–1542. https://doi.org/10.1089/CMB.2011.0184.

68. Hofacker, I.L. (2003). Vienna RNA secondary structure server. Nucleic Acids Res. 31, 3429–3431. https://doi.org/10.1093/nar/gkg599.

69. Lorenz, R., Bernhart, S.H., Höner zu Siederdissen, C., Tafer, H., Flamm, C., Stadler, P.F., and Hofacker, I.L. (2011). ViennaRNA Package 2.0. Algor. Mol. Biol. 6, 1–14. https://doi.org/10.1186/1748-7188-6-26/TABLES/2.

70. Afonine, P.V., Poon, B.K., Read, R.J., Sobolev, O.V., Terwilliger, T.C., Urzhumtsev, A., and Adams, P.D.; IU (2018). Real-space refinement in PHENIX for cryo-EM and crystallography. Acta Crystallogr. D Struct. Biol. *74*, 531–544. https://doi.org/10.1107/S2059798318006551.

71. Lang, B., Armaos, A., and Tartaglia, G.G. (2019). RNAct: protein-RNA interaction predictions for model organisms with supporting experimental data. Nucleic Acids Res. *47*, D601–D606. https://doi.org/10.1093/NAR/GKY967.

72. Fu, T.F., Rife, J.P., and Schirch, V. (2001). The role of serine hydroxymethyltransferase isozymes in one-carbon metabolism in MCF-7 cells as determined by (13)C NMR. Arch. Biochem. Biophys. *393*, 42–50. https://doi.org/10.1006/ABBI.2001.2471.

73. Hernández, H., and Robinson, C.V. (2007). Determining the stoichiometry and interactions of macromolecular assemblies from mass spectrometry. Nat. Protoc. *2*, 715–726. https://doi.org/10.1038/nprot.2007.73.

74. Quetschlich, D., Esser, T.K., Newport, T.D., Fiorentino, F., Shutin, D., Chen, S., Davis, R., Lovera, S., Liko, I., Stansfeld, P.J., et al. (2021). NaViA: a program for the visual analysis of complex mass spectra. Bioinformatics *37*, 4876–4878. https://doi.org/10.1093/bioinformatics/btab436.

75. Marty, M.T., Baldwin, A.J., Marklund, E.G., Hochberg, G.K.A., Benesch, J.L.P., and Robinson, C.V. (2015). Bayesian deconvolution of mass and ion mobility spectra: from binary interactions to polydisperse ensembles. Anal. Chem. *87*, 4370–4376. https://doi.org/10.1021/acs.analchem.5b00140.

76. Giardina, G., Brunotti, P., Fiascarelli, A., Cicalini, A., Costa, M.G.S., Buckle, A.M., Di Salvo, M.L., Giorgi, A., Marani, M., Paone, A., et al. (2015). How pyridoxal 5′-phosphate differentially regulates human cytosolic and mitochondrial serine hydroxymethyltransferase oligomeric state. FEBS Journal *282*, 1225–1241. https://doi.org/10.1111/febs.13211.

77. Scarsdale, J.N., Radaev, S., Kazanina, G., Schirch, V., and Wright, H.T. (2000). Crystal structure at 2.4 A resolution of E. coli serine hydroxymethyltransferase in complex with glycine substrate and 5-formyl tetrahydrofolate. J. Mol. Biol. *296*, 155–168. https://doi.org/10.1006/JMBI.1999.3453.

78. Jones, D.T., Taylor, W.R., and Thornton, J.M. (1992). The rapid generation of mutation data matrices from protein sequences. Comput. Appl. Biosci. *8*, 275–282. https://doi.org/10.1093/bioinformatics/8.3.275.

79. Tamura, K., Stecher, G., and Kumar, S. (2021). MEGA11: Molecular Evolutionary Genetics Analysis Version 11. Mol. Biol. Evol. *38*, 3022–3027. https://doi.org/10.1093/molbev/msab120.

80. Stecher, G., Tamura, K., and Kumar, S. (2020). Molecular evolutionary genetics analysis (MEGA) for macOS. Mol. Biol. Evol. *37*, 1237–1239. https://doi.org/10.1093/molbev/msz312.

## STAR★METHODS

### KEY RESOURCES TABLE

| REAGENT or RESOURCE | SOURCE | IDENTIFIER |
|---|---|---|
| **Bacterial and virus strains** | | |
| BL21 (DE3) *E. coli* | New England Biolabs | C2527H |
| **Biological samples** | | |
| pET28b(+) vector | Novagen | 69744-3 |
| pCMV3 vector | Sino Biological | CV011 |
| **Chemicals, peptides, and recombinant proteins** | | |
| Luria Broth medium | Fisher Scientific | BP1426-2 |
| Isopropyl β-D-1-thiogalactopyranoside | Merck | 367-93-1 |
| Bovine serum albumin (BSA) | Merck | 9048-46-8 |
| Thrombin | Merck | 9002-04-4 |
| diethyl pyrocarbonate (DEPC) | Merck | 1609-47-8 |
| serine | Merck | 56-45-1 |
| glycine | Merck | 56-40-6 |
| Imidazole | Merck | I202 |
| Ethylenediaminetetraacetic acid | Merck | E9884 |
| Boric Acid | Carlo Erba | 402767 |
| 2-Amino-2-(hydroxymethyl)-1,3-propanediol | Merck | TRIS-RO |
| Sodium Chloride | Merck | S9625 |
| Cytiva HisTrap FF Columns | Merck | GE17-5255-01 |
| QuikChange Lightning Site-Directed Mutagenesis Kit | Agilent | 210519 |
| SYBR™ Safe DNA Gel Stain | ThermoFisher | S33102 |
| Phosphate Buffered Saline Tablets | Merck | 524650 |
| Tween 20 | Merck | P9416-100ML |
| Trypsin-EDTA (0.25%) in HBSS (1x), with Phenol Red | yourSIAL | SIAL-TryEDTA |
| Dulbecco's PBS (1x) | Sigma-Aldrich | D8537 |
| Fetal Bovine Serum | ThermoFisher | A5256701 |
| RPMI 1640 Medium, with L-Glutamine | yourSIAL | SIAL-RPMI-A |
| Iscove's Modified Dulbecco's Medium, with L-Glutamine | yourSIAL | SIAL-IMDM-A |
| HT Supplement (100X) | ThermoFisher | 11067030 |
| Penicillin/Streptomycin (100X) | yourSIAL | SIAL- PEN/STREP |
| Hygromycin B (50 mg/mL) | ThermoFisher | 10687010 |
| jetPRIME® transfection kit | Polyplus | 101000015 |
| 1,4 Dithiothreitol (DTT) | Sigma-Aldrich | D9779 |
| NuPAGE™ 4 to 12%, Bis-Tris, 1.0–1.5 mm, Mini Protein Gels | ThermoFisher | NP0323BOX |
| IBLOT 2NC REGULAR STACKS | ThermoFisher | IB23001 |
| CelLytic™ M | Sigma-Aldrich | C2978 |
| Pierce™ BCA Protein Assay Kits | ThermoFisher | 23225 |
| MOPS, 99%, Thermo Scientific Chemicals | ThermoFisher | A12914-22 |
| Clarity Western ECL Substrate | BioRad | 1705061 |
| PageRuler™ Plus Prestained Protein Ladder, 10 to 250 kDa | ThermoFisher | 26619 |

*Continued*

| REAGENT or RESOURCE | SOURCE | IDENTIFIER |
|---|---|---|
| Water molecular biology reagent | Sigma-Aldrich | w4502-1L |
| **Deposited data** | | |
| Atomic model of SHMT1:RNA complex | This paper | PDB: 8A11 |
| Cryo-EM map of SHMT1:RNA complex | This paper | EMDB: EMD-15065 |
| Atomic model of SHMT1 | This paper | PDB: 8R7H |
| Cryo-EM map of SHMT1 | This paper | EMDB: EMD-18973 |
| **Oligonucleotides** | | |
| RNA UTR2$_{1-50}$ (Cryo-EM) | Eurofins Genomics | Custom made |
| RNA UTR2 $_{1-50}$ and UTR2 $_{1-50 Rv}$ | Biomers.net | Custom made |
| RNA UTR2 loop length 6 nt and UTR2 loop lenght 24 nt | Eurofins Genomics | Custom made |
| **Antibodies** | | |
| Mouse monoclonal mSHMT (F-11) antibody | Santa Cruz | AB_2920890 |
| Mouse IgG$_K$ BP-HRP | Santa Cruz | AB_2687626 |
| **Experimental models: cell lines** | | |
| HAP1 (MALE) | Horizon Discovery | Cat#C631; RRID: CVCL_Y019 |
| A549 (Sex unspecified) | Giardina et al.[19] | N/A |
| **Software and algorithms** | | |
| RELION-3.0 | Zivanov et al.[54] | https://www2.mrc-lmb.cam.ac.uk/relion/index.php/Main_Page |
| PHENIX | Adams et al.[55] | https://phenix-online.org |
| Coot | Emsley et al.[56] | https://www2.mrc-lmb.cam.ac.uk/personal/pemsley/coot/ |
| UCSF CHIMERA | Pettersen et al.[57] | http://www.cgl.ucsf.edu/chimera |
| Image Lab | BioRad | https://www.bio-rad.com/de-de/product/image-lab-software?ID=KRE6P5E8Z |
| Prism GraphPad | GraphPad Software | Version 8 |
| **Other** | | |
| Grids | Quantifoil | Three-hundred mesh holey gold R0.6/1 and R1.2/1.3 |

## RESOURCE AVAILABILITY

### Lead contact
Further information and requests for resources and reagents should be directed to and will be fulfilled by the lead contact, Francesca Cutruzzolà (Francesca.cutruzzola@uniroma1.it).

### Materials availability
Chemicals and reagents serine, glycine, bovine serum albumin (BSA), thrombin, diethyl pyrocarbonate (DEPC), and all the salts were obtained from Merck. Tetrahydrofolate and (6S)-5-formyl tetrahydrofolate (monoglutamylated forms) were kindly provided by Merck & Cie (Schaffhausen, Switzerland). All other chemicals were used in the enzymatic assays purchased from Sigma-Aldrich.UTR2 $1_{-50}$ used for the cryo-EM experiments was purchased from Eurofins Genomics (Germany GmbH), instead the UTR2$_{1-50}$ and UTR2$_{1-50}$ Rv used for in vitro experiments was purchased from biomers.net GmbH 2023. UTR2 loop length 8nt and UTR2 loop length 28nt were purchased from Sigma-Aldrich. All unique/stable reagents generated in this study are available from the lead contact with a completed materials transfer agreement.

### Data and code availability
- Cryo-EM density maps of the SHMT1:RNA complex and SHMT1 protein used in model building have been deposited in the Electron Microscopy Data Bank (EMDB) under the following accession numbers: EMD-15065 (SHMT1:RNA), EMD-18973 (SHMT1). Atomic coordinates have been deposited in the Protein Data Bank (PDB) with the accession numbers PDB: 8A11 (SHMT1:RNA) and PDB: 8R7H (SHMT1). The deposited datasets will be publicly available upon publication.
- This paper does not report original code.
- Any additional information required to reanalyze the data reported in this paper is available from the lead contact upon request.

## EXPERIMENTAL MODEL AND STUDY PARTICIPANT DETAILS

### Cell lines culture and transfection

A549 and HAP1, respectively lung and leukaemia cancer cells, were grown at 37°C and 5% $CO_2$ in RPMI-1640 and IMDM media supplemented with 2 mM-glutamine, 100 IU·mL−1 penicillin/streptomycin and 10% foetal calf serum (Sigma-Aldrich). For HAP SHMT1 knockout IMDM medium was supplemented with GIBCO HT Supplement 1X (Sigma-Aldrich). For HAP SHMT1 knockout rescued SHMT1 wild type and SHMT1 mutants, hygromycin B was added in IMDM medium for the selection with a concentration of 500μg/ml supplied by ThermoFisher Scientific.

Transient or stable transfection experiments were carried out by seeding A459 and HAP SHMT1 knock out cells ($1 \times 10^5$ cells per plate) in six-well dishes in complete RPMI-1640 or IMDM medium respectively. Transfection was performed adding 1 μg per well of pCMV3-DNA, pCMV3-DNA_SHMT1 or pCMV3-DNA_SHMT1 K279S plasmids 24 h after plating using JetPrime™ (Polyplus transfection, Illkirch, France) reagent following the manufacturer's instructions. Transfection medium was replaced with complete RPMI-1640 or IMDM medium after 12 h. Cells were not authenticated and they derived from ATCC.

## METHOD DETAILS

### Protein expression and purification

Wild-type and mutants (K282S, R393S-R397S, K279S) SHMT1 genes were cloned into a pET22b(+) vector (Novagen) and expressed as N-terminal histidine-tagged fused protein in *Escherichia coli* (BL21-DE3). Bacterial cultures were grown at 37 °C in Luria-Bertani (LB) liquid medium supplemented. Purification was performed as previously described by Spizzichino et al.[58] Briefly, bacterial pellets were then resuspended in a lysis buffer (20mM Hepes pH 7.2; 150 mM NaCl; 5% glycerol) and lysed by ultrasonic disruption on ice. Soluble proteins were purified by IMAC on a $Ni^{2+}$-His- Trap column (Cytiva, Chicago, IL, USA). SHMT1 eluted with 300 mM imidazole. Fractions containing pure protein were pooled, and imidazole was removed with desalting columns PD10 (Cytiva, Chicago, IL, USA), the histidine tag was then removed by proteolytic digestion with 1U/mg of thrombin (SIGMA). The digestion mixture was then loaded again on the IMAC on a $Ni^{2+}$-His-Trap column (Cytiva, Chicago, IL, USA) and SHMT1, which now binds with low affinity, was eluted with 100 mM imidazole. The protein was injected into a Superdex 200 column (16/600; GE Healthcare) and eluted as a tetramer with the following buffer, 20mM Hepes pH 7.2; 150 mM NaCl; 5% glycerol. Protein concentration was determined by measuring the absorbance at 280 nm and applying the Beer-Lambert law (SHMT1 $\varepsilon_{280}$ 47565 $M^{-1}cm^{-1}$). Samples were frozen in liquid nitrogen and stored at -20 °C.

### Site directed mutagenesis

SHMT1 mutants were produced by site-directed mutagenesis using the QuikChange Lightning Site-Directed Mutagenesis Kit (210518, Agilent Technologies). The pET28b and pCMV3 (Sino Biological) containing the wild-type SHMT1 were used as template DNA. Two complementary oligonucleotides, synthesised by Eurofins, were used as primers for the mutagenesis reactions. Escherichia coli Neb5α cells were transformed to amplify the mutated plasmids and mutagenesis were verified by sequencing. pET28b plasmids containing either SHMT1 WT or SHMT1 mutants were used for purification of proteins employed to perform all the in vitro experiments. pCMV3 plasmids containing either SHMT1 WT or SHMT1 mutants were used to obtain the overexpression of the proteins in the *in cellulo* experiments.

### Cryo-EM grid preparation and data acquisition

To reduce the RNA molecule mobility and to increase the homogeneity of the single particle on the grids, downsizing of the 5'UTR region of SHMT2 mRNA was necessary. A 50 nt fragment ($UTR2_{1-50}$) was selected as a tool to see the complex formation in cryo-EM since this fragment showed, amongst all the tested RNA oligonucleotides, the highest binding affinity to SHMT1 and was still able to decrease enzyme activity *in vitro* (Figures S4B and S4D).

Purified SHMT1 protein at 0.3 mg/ml concentration in 150 mM NaCl, 20 mM Hepes pH 7.2 buffer, was incubated with $UTR2_{1-50}$ RNA at a 1:5 protein:RNA molar ratio. A 3 μl drop of the sample was applied to glow-discharged Quantifoil 1.2/1.3 300 mesh Cu grids for 20 s and blotted before plunge-freezing in liquid ethane. Grid vitrification was performed using a Vitrobot Mark IV (Thermo Fisher Scientific) at 100% humidity and 4°C.

A total of 5,450 movies were collected on a Talos Arctica microscope (Thermo Fisher Scientific) operating at 200 kV on a Falcon 3EC camera in electron counting mode. The dataset was automatically acquired using EPU software (Thermo Fisher Scientific). The pixel size was set to 0.889 Å/pixel. Each movie consists of 40 frames with a total accumulated dose is 40 $e^-/Å^2$. Applied defocus ranged between -0.5 and -2.5 μm.

### Single-particle data processing

Movies were motion corrected and dose weighted with MotionCor2 implemented in Relion 3.1.[54] CTF estimation was performed with CTFFIND-4.1.13 using the sums of power spectra from combined fractions.[59] Images were processed using RELION 3.1.[54] A first subset of 10 representative micrographs was subjected to LoG autopicking. After 2D classification, classes with low background were selected and used as models for a 2D-reference based Autopicking on the whole dataset. A total of 4.9 million initial particles were picked and then subjected to multiple rounds of 2D classification. After generating a low-pass filtered initial model from the SHMT1

crystallographic structure (PDB: 6FL5), selected class averages with high resolution features (0.9 million particles) were subjected to a first round of 3D classification with C1 symmetry to remove remaining junk particles. of the remaining 0.7 M particles, a second round of 3D classification with C1 symmetry revealed classes with an extra-density located at one out of the four nucleotide-binding sites of SHMT1. Despite the symmetry of SHMT1 homotetramer, we avoided applying any kind of symmetry bias. Selected classes containing similar extra-densities or the putative RNA-freeform were separately grouped and subjected to further 3D classification to select a subset of homogeneous particles. Final 3D classes selected contained 94,430 and 73,523 particles for the RNA-bound and the RNA-free states respectively. These were subjected to masked 3D auto-refinement, CTF refinement and Bayesian polishing in Relion. The estimated resolution of the final maps, following standard post-processing procedures in RELION,[60] was 3.52 Å for the RNA-bound SHMT1 and 3.29 Å for the RNA-free state. An overall scheme of the image processing pipeline is presented in Figure S1.

### Local scale map sharpening

Local map sharpening was performed using a model-free implementation of the software LocScale.[54] The original implementation of LocScale utilizes information on the amplitude of the radially averaged structure factor computed locally from an atomic model with refined atomic displacement (ADP) factors. In the model-free implementation used here, which is available at https://gitlab.tudelft.nl/aj-lab/locscale,[61] no prior model information is employed and the radial structure factor is instead approximated by a composite radial profile consisting of a shape-dependent fall-off in the low resolution region (infinity to $\sim0.1$ Å$^{-1}$) that is defined by the molecular envelope, and a generalised radial structure factor scaled by the local B factor estimated from the Wilson region ($\sim0.1$ Å$^{-1}$ to Nyquist frequency).

The general theoretical basis for this procedure has been described in detail previously[62] and is invoked within LocScale using the command:

np_locscale.py -em [unsharpened_map.mrc] -r 4.3 -p 0.889 -bl 1.2 -it 100 -w 40 -fdr_w 40 -pm random_placement_with_kick -o [locscale_map.mrc] -v True

This command constructs the sharpened density by locally applying the scaling procedure in the Fourier domain over local regions in the real space map sampled in a rolling window of 40x40x40 pixels. Briefly, for each grid step, the unfiltered experimental density map contained within the rolling window was sharpened by a resolution-dependent amplitude scaling factor as $F_{corr}(s) = k(s)F_{obs}(s)$, where $F_{obs}(s)$ is the Fourier amplitude of the experimental density map at spatial frequency s, and k(s) a frequency-dependent scaling factor constructed as described above. After inverse Fourier-transforming, the real-space map value of the central voxel contained in the scaled volume element was then assigned to the corresponding voxel of the new map. Repeating the procedure over each voxel position yielded the locally sharpened map.

### Model building

The initial models of the SHMT1-RNA complex and unbound SHMT1, whereas generated performing a rigid body fit of SHMT1 crystal structure (PDB: 1BJ4 [22]) by using UCSF Chimera.[57] Each subunit was fitted independently. The initial model was then manually modified and refined in Coot[56] to fit the sharpened map or, in the more dynamic regions, the unsharpened one. In both structures the PLP cofactor and surrounding residues (147-152) were removed from the chains with electron density lacking in the active site, to clearly distinguish the open and closed conformations. For subunit D of the complex the same residues were retained but with an occupancy of 0.5 to account to the lower density observed. To aid RNA model building the UTR2$_{1-50}$ secondary structure was predicted using 6 different servers: *CentroidFold*,[63] *CONTRAFold*,[64] *IPknot*,[65] *RNAstructure*,[66] *ContextFold*[67] and *RNAfold*[68,69]). The first 4 predicted the same ss that was then fed to the RNA *composer* server to predict the 3D structure. The hairpin region of the predicted structure nicely fitted the "rugby ball" shaped RNA density. A maximum of 6 nucleotides belonging to this region could be placed into the extra electron density and refined with good geometry, correlation coefficients and B-factor values. However, multiple orientations of the RNA model could be fitted and refined with similar values. Therefore, given the uncertainty of the correct pose (likely an ensemble of multiple conformations/orientations), RNA was not included in the final model of the complex.

The full atomic models of SHMT1-RNA complex and SHMT1 unbound were then subjected 3 cycles of real-space refinement using PHENIX,[55] including global minimization and refinement of atomic displacement parameters, and applying secondary structures, Ramachandran, and nucleic acids restraints.[70] Full statistics are reported in Table 1.

### catRAPID

The interaction between UTR2$_{1-50}$ stretches and SHMT1 was predicted using catRAPID.[41] CatRAPID estimates the binding potential through van der Waals, hydrogen bonding and secondary structure propensities of both protein and RNA sequences, allowing identification of binding partners with high confidence. As an analysis of about half a million of experimentally validated interactions[71] the algorithm can separate interacting vs. non-interacting pairs with an area under the curve (AUC) receiver operating characteristic (ROC) curve of 0.78 (with false discovery rate (FDR) significantly below 0.25 when the Z-score values are >2). SHMT regions of 100 residues with a 50-residue overlap were employed in the calculations.

### EMSA assays

EMSA assays were used to assess the binding affinity of different RNAs towards SHMT1, and the ability of the mutants to bind RNA. These experiments were conducted by incubating a fixed amount of RNA (*0.24 μM*) with either fixed or increasing concentrations of purified SHMT1 (or variants; 0.5 to 9.6 *μM*).

All the components were incubated at 25°C for 30 minutes in 12 μl of binding buffer (20 mM HEPES pH 7.4, 100 mM NaCl) containing 20 μg/ml bovine serum albumin (BSA) and 8% (v/v) glycerol. The reaction mixtures were then subjected to electrophoresis under native conditions using a non-denaturing 4% polyacrylamide gel in 0.5× TBE buffer (45 mM Tris-Borate, 1 mM ethylenediaminetetraacetic acid pH 8.6). For the visualisation, gels were stained with SYBR Safe (Invitrogen) in 30 ml of 0.5× TBE and images were acquired using Chemidoc MP Imaging System (Bio-Rad). Densitometric measurements of the free RNA bands were transformed into percentages, the amount of bound RNA (% bound) was then calculated by subtracting the percentage of free RNA from the total, the result was plotted as a function of protein concentration. The apparent dissociation constant (KD) was estimated fitting the data with Equation 1, in which Bmax corresponds to the maximum binding (100%) and [P] corresponds to the concentration of SHMT1 in the reaction mixture.

$$\% \ Bound \ = \ B_{max}\frac{[P]}{K_d+[P]}$$

(Equation 1)

### Activity assays

All assays were carried out at 30 °C in 20 mM K-phosphate buffer at pH 7.2, treated with diethyl pyrocarbonate (DEPC). The serine cleavage reaction was measured using 0.2 μM of purified SHMT1 with fixed 10 mM L-serine and 50 μM THF as substrates while varying the RNA concentration. A spectrophotometric coupled assay, in which the 5,10-methylene-THF produced by the reaction was oxidized by the NAD-dependent *E. coli* 5,10-methylene-THF dehydrogenase was used.[72]

All obtained inhibition curves were fitted to the equation below, in which [I] corresponds to the RNA concentration:

$$\%Activity \ = \ 100\cdot\left(1 \ - \ \frac{[I]}{[I]+IC50}\right)$$

(Equation 2)

The inhibition kinetics of the SHMT1 by $UTR2_{1-50}$ RNA was carried out as described in Guiducci et al.,[21] using $UTR2_{1-50}$ RNA in the place of tRNA. The single saturation curves obtained keeping L-serine concentration constant at 10 mM and varying THF (between 3 and 485 μM) at various $UTR2_{1-50}$ RNA concentrations (0, 0.24 e 1.2 μM) were fitted to a modified Michaelis-Menten equation that accounts for substrate inhibition.

$$v_i \ = \ v_{max}\frac{[THF]}{K_m+[THF]\left(1+\frac{[THF]}{K_i}\right)}$$

(Equation 3)

All spectrophotometric measurements were performed using a Hewlett Packard 8453 diode-array spectrophotometer. Fitting of data to equations was carried out with the PRISM software (GraphPad, La Jolla, CA, USA).

### Spectral measurements of SHMT1-amino acid complexes

All SHMT1-amino acid spectra were recorded at 25°C in 50mM Hepes buffer, 150mM NaCl, 5% glycerol at pH 8, in the 260-600 nm range, using Jasco V-650 spectrophotometer. After 30 minutes of incubation at 25°C of $UTR2_{1-50}$ RNA 1:4 SHMT1 18 μM, final concentrations of 10mM serine or glycine respectively were added to the cuvette with 1 cm path length. For the negative control, water with the same volume of RNA solution was added. Acquired spectra were normalised with the respective baseline (SHMT1 buffer) with IgorPro 8 software (Wavemetrics, Lake Oswego, OR, USA) and the differential spectra in the PLP absorption region (315-500 nm) for each experiment were calculated with PRISM software (GraphPad, La Jolla, CA, USA).

### Differential Scanning Fluorimetry (DSF)

DSF assays were performed on a Real Time PCR Instrument (CFX Connect Real Time PCR system, Bio-Rad) using 96-well PCR plates. In each well 1 μM SHMT1 or K279S in 20 mM K-phosphate buffer, pH 7.2, and Sypro Orange (2.5x, Thermo Scientific) were mixed in a total volume of 25 μL with various ligands (CHO-THF-5Glu, CHOTHF, lometrexol, $UTR2_{1-50}$) in a 96-well PCR plate. Fluorescence was measured from 25°C to 95°C in 0.4°C/30 sec steps (excitation 450-490 nm; detection 560-580 nm). All samples were run in triplicate. Denaturation profiles were analysed using Graph Pad software after removal of points representing quenching of the fluorescent signal due to postpeak aggregation of protein:dye complexes. All curves were normalised and fitted to a sigmoidal equation to obtain the melting temperatures (Tm). Alternatively, Tm values were obtained by plotting the first derivative of the fluorescence emission as a function of temperature (-dF/dT) by using the Bio-Rad CFX manager software.

### Native MS analysis

Protein samples were buffer exchanged into 500 mM ammonium acetate (pH 7.2) via a PD-10 column followed by overnight dialysis at 4°C prior to native MS analyses. The RNA sample was diluted in 500 mM ammonium acetate (pH 7.2). For RNA binding experiments, an RNA stock solution in 500 mM ammonium acetate was added to the protein solution to have a final RNA concentration of 8 μM and final protein concentration of 2 μM. The mixture was then incubated at room temperature for 20 minutes prior to native

MS analysis. We tried to perform the experiment also for the double mutant R393S-R397S but it precipitates in the ammonium acetate buffer required for the analysis.

The samples were directly introduced into the mass spectrometer using gold-coated capillary needles prepared in-house.[73] Data were collected on a Q Exactive UHMR Hybrid Quadrupole-Orbitrap mass spectrometer (Thermo Fisher) in negative polarity. The instrument parameters used for MS spectra collection were the following: capillary voltage 1.0 kV, scan range from 1,000 to 20,000 m/z, HCD collision energy 150 V, source fragmentation 0 V, in-source trapping 100 V. The ion transfer optics was set as follows: injection flatapole -5 V, inter-flatapole lens -4 V, bent flatapole -2 V, transfer multipole 0 V. The resolution of the instrument was 8,750 at m/z = 200 (transient time of 64 ms), nitrogen pressure in the HCD cell was maintained at approximately $5.5 \times 10 -10$ mbar and transfer tube temperature were kept at $100°C$. The noise level was set at 3 rather than the default value of 4.64. Calibration of the instruments was performed using a solution of caesium iodide (2 mg/mL) in water.

Data were analysed using the Xcalibur 3.0 (Thermo Scientific), NaViA[74] and UniDec.[75] Software packages and the quantified RNA-bound protein were plotted using GraphPad Prism 8.0. Statistical significance was calculated via unpaired t-test (Welch's correction).

### Trypsin digestion

SHMT1 WT ($2\mu M$) was incubated with UTR2$_{1-50}$ ($10\mu M$) for 30 minutes at room temperature. Afterwards, 0.04 $\mu g/\mu l$ of trypsin (diluted in ammonium bicarbonate pH 7.6) were added and the reaction was stopped at the given times (0 min, 10 min, 30 min, 1h, 2h, overnight) by adding Invitrogen™ NuPAGE™ LDS Sample Buffer (4X) and boiling samples for 10 minutes.[76]

Samples were then runned in a SDS denaturing gel and the image was acquired at Chemidoc MP Imaging System (Bio-Rad). Densitometric measurements of the bands were performed by using Image Lab software (Bio-Rad). Statistics were performed by using the unpaired t-test analysis. Selected bands were submitted to trypsin proteolysis. Briefly, after few washing steps with a 50 mM of ammonium bicarbonate with/without 50% of acetonitrile and pure acetonitrile solution, and next carbamidomethylation with 55 mM Iodoacetamide (IAA), the proteolysis was carried out with 100ng of trypsin in 25 mM of ammonium bicarbonate, with the addition of 0.01% ProteaseMAX™ Surfactant, Trypsin Enhancer (Promega), at $50°C$ for 1h. The tryptic mixtures were analyzed by an ultrafleXtreme MALDI ToFToF (Bruker, Bremen DE), equipped with a smartbeam-II laser.

### Protein extracts, SDS-PAGE and Western Blotting

After cells lysis in 8 M urea (Sigma-Aldrich), 40 $\mu g$ of proteins (protein concentration determined by Pierce BCA Protein Assay Kit (Thermo Fisher Scientific) were separated by SDS/PAGE and transferred to a nitrocellulose membrane, which was then saturated with 5% BSA in Tris-buffered saline with 0.1% Tween 20. Membranes were incubated with primary antibody for 18 h at 4 °C; horseradish peroxidase-conjugated secondary antibody for 1h at RT; washed with Tris-buffered saline in 0.1% Tween 20 and developed using the chemiluminescence system Chemidoc MP Imaging System (Bio-Rad). Antibody anti-SHMT2, -β-actin and the secondary antibodies anti-mouse were from Santa Cruz Biotechnology (Dallas, TX, USA). Densitometry has been performed with Image Lab software by Bio-Rad. The percentages of SHMT2 expression plotted in the histograms under various conditions were calculated using densitometry which was normalised to their respective actin levels. In the transiently transfected A459 cell line, the endogenous SHMT1 is present in all samples, including those overexpressing SHMT1 WT or the K279S mutant.

### Phylogenetic Analysis

We assessed the presence of the flap motif and, at the same time, of the three major residues responsible for the tetramerization in human SHMT1, i.e., His 135, Arg 137, and Glu 168[22,19] by modelling SHMT structures from a total of 25 representative species (Figures S6, S7A, and S7B; Table S5). All the crystal structures and AlphaFold2 models obtained were compared to the crystal structures of SHMT from *E. coli* (PDB: 1DFO [77]), and from *H. sapiens* (PDB: 1BJ4[22]).

The evolutionary analysis was inferred by using the Maximum Likelihood method and JTT matrix-based model.[78] The tree with the highest log likelihood is shown in Figure S10. Initial tree(s) Evolutionary analyses were conducted in MEGA11.[79,80] The multiple sequence alignment of the flap motif was built by comparing the topologically equivalent residues of the superposed SHMT available crystal structures and AlphaFold2 models.

### QUANTIFICATION AND STATISTICAL ANALYSIS

The western blot and EMSA images were analysed with ImageLab (Bio-Rad, Califormia) and the data from at least three independent experiments were averaged. Statistical analysis was performed using Prism 8.0 (GraphPad Software). All quantitative data are presented as the mean ± SD. Statistical significance throughout the experiments is indicated in the relative figure legend and was calculated via unpaired t-test (Welch's correction).